CCFE
CULHAM CENTRE FOR FUSION ENERGY

UK Atomic Energy Authority

UKAEA-CCFE-PR(21)15

Viacheslav Kuksenko, Artem Lunev, Ed Darnbrough,
Chris Densham, Patrick Hurh, Steve Roberts

Radiation induced hardening of beryllium during low temperature He implantation

Radiation induced hardening of beryllium during low temperature He implantation

Viacheslav Kuksenko, Artem Lunev, Ed Darnbrough, Chris Densham, Patrick Hurh, Steve Roberts

This is a preprint of a paper submitted for publication in Journal of Nuclear Materials

CCFE
CULHAM CENTRE FOR FUSION ENERGY

UK Atomic Energy Authority

UKAEA-CCFE-PR(21)15

Viacheslav Kuksenko, Artem Lunev, Ed Darnbrough,
Chris Densham, Patrick Hurh, Steve Roberts

Radiation induced hardening of beryllium during low temperature He implantation

Radiation induced hardening of beryllium during low temperature He implantation

Viacheslav Kuksenko, Artem Lunev, Ed Darnbrough, Chris Densham, Patrick Hurh, Steve Roberts

This is a preprint of a paper submitted for publication in Journal of Nuclear Materials

Radiation induced hardening of beryllium during low temperature He implantation

Viacheslav Kuksenko[1), 2)], Artem Lunev[1)], Ed Darnbrough[2)], Chris Densham[3)], Patrick Hurh[4)], Steve Roberts[1)]
[1)] UK Atomic Energy Authority, Abingdon, UK
[2)] University of Oxford, Oxford, UK
[3)] Rutherford Appleton Laboratory, Didcot, UK
[4)] Fermi National Accelerator Laboratory, Batavia, USA

** Corresponding author:slava.kuksenko@ukaea.uk*

Abstract

The effect of ion irradiation on evolution of microstructure and hardening of beryllium with different impurity levels was investigated using TEM and nanoindentation. High purity S-65 nuclear beryllium grade and lower-pure S-200-F structural beryllium grade were implanted by helium ions at temperatures of 50ºC and 200ºC. 11 different energies were used, so as to create a quasi-homogeneous 3μm irradiated layer with average radiation damage of 0.1dpa and average He content of 2000 appm.

At both temperatures in both grades, under TEM investigation the radiation damage appears as "black dots" (<10 nm in diameter) which are likely to be small dislocation loops with the number density of ~ 10^{22} m^{-3}. No bubbles were observed inside grains and at grain boundaries.

Nanoindentation experiments demonstrated that the lower-purity S-200-F grade has higher average hardness (3.7±0.8 GPa) than the S-65 grade (3.4±0.8 GPa) in the as-received and irradiated states. After helium implantation of both grades the hardness increased by 60% for the 200ºC irradiation and 100% for the 50ºC irradiation. The higher purity S-65 grade showed smaller changes in hardness at 200ºC than the less pure S-200-F. Use of EBSD to give the crystallographic orientation of indented grains revealed that in both grades in the as-received materials the hardness is about 2.5 times higher when the indentation direction is close to the [0001] c-axis of beryllium compared to indentation perpendicular to [0001]. Hardness anisotropy significantly decreased after irradiation: the "soft orientation" was most sensitive to radiation-induced hardening, with hardness increasing by about 140% after irradiation at 50ºC and 100% after irradiation at 200ºC, compared to about 15 - 20% for the "hard" orientation at both irradiation temperatures.

Analysis of the possible hardening contribution demonstrated that the "back dots" should lead to about 0.85 and 1.7 GPa hardness increase, while the rest of the hardening should originate from helium bubbles with the size below the TEM resolution (at or below 1.5 nm).

Key words: beryllium, helium implantation, radiation hardening, anisotropy, TEM

1. Introduction

Due to a unique combination of mechanical and physical properties, beryllium is extensively used in a wide variety of nuclear facilities. For example, due to its high thermal conductivity, low chemical sputtering and oxygen gettering properties [1], beryllium is a plasma facing material (PFM) for the Joint European Torus (JET) tokomak [2,3] and the future ITER fusion test reactor [4,5]. Beryllium is also being considered as a neutron multiplier material in the helium-cooled pebble bed (HCPB) design concept for the tritium-breeding blanket of the demonstration fusion power plant (DEMO) [6,7]. Due to its low nuclear interaction cross-section, beryllium is an excellent material for particle-beam windows, and, for example, was successfully used as a primary beam window in neutrino production targets of the "Neutrinos at the Main Injector" (NuMI) beamline [8]. It is also being considered as a material for different target components in a new generation of proton accelerator driven particle sources such as, for example, the Long Baseline Neutrino Facility (LBNF) [9,10].

In comparison to other nuclear materials, beryllium experiences extremely high transmutant helium accumulation rate. For example, it is between 110 and 220 appm/dpa in the beryllium reflector of the ISIS neutron source (RAL, UK) and can reach 380 He-appm/dpa under neutron irradiation in fission reactors [11–13]. For comparison, a typical appm/dpa ratio for iron under neutron irradiation in fission pressurized-water reactor (PWR) is 0.35 appm/dpa [14] and for tungsten under neutron irradiation in fission high flux isotope reactor (HFIR) is 0.0008 appm/dpa [15]. In fusion reactors, beryllium will accumulate helium with the rate of 670 He-appm/dpa [14] that will lead to build-up of 1,500 He-appm at ITER end-of-life [16] and more than 15,000 He-appm at DEMO end-of-life (HCPB concept) [17]. Even higher helium accumulation, up to 4000 He-appm/dpa, takes place in beryllium in high energy proton irradiation environments, for example in neutrino sources [18]. Both helium accumulation and displacement damage effects in beryllium are known to be highly irradiation-temperature dependent: for temperatures less than 400ºC, radiation induced hardening accompanied with a drop in plasticity is usually observed, whereas severe non-hardening embrittlement is observed

for high-temperature irradiation [19–22]. It is generally considered that the determining mechanisms here are strengthening of the beryllium matrix by point defect clusters and helium accumulation at low temperatures; and helium segregation to grain boundaries at high temperatures [12,22–24].

Industrial purity beryllium grades used in nuclear facilities contain a wide variety of trace impurities, typically oxygen, iron, aluminium, nickel, copper, silicon, carbon and magnesium. The majority of these impurities have very limited solubility in beryllium, and have strong tendencies to create precipitates and to segregate to defects such as grain boundaries or dislocations [18,25]. While the effects of different impurities on mechanical properties of beryllium have been extensively studied in the past (see reviews [7,25] and references sited), the mechanisms underlying these processes are not always well understood. Moreover, data about the effects of impurities on evolution of mechanical properties under radiation is very limited, especially under the extreme conditions relevant to beryllium components of fusion reactors and particle accelerators.

The work reported here compares hardening introduced by helium implantation in two industrial beryllium grades: the high purity nuclear grade S-65 and the lower-purity structural grade S-200-F. The S-65 grade is being used as a plasma-facing component in Joint European Torus fusion experiment [3] and was selected as the reference material for use in ITER [7]. The S-200-F grade is also used in nuclear facilities, for example for beryllium frames and reflector elements in the Japan Materials Testing Reactor (JMTR) at JAEA [26].

We report data on irradiation hardening effects in beryllium at 50ºC and 200ºC. The temperatures represent the lower boundary of the expected irradiation temperatures in Be for ITER first-wall applications, and typical irradiation temperatures of the beryllium in the operating NuMI neutrino target [18] and the currently designed LBNF [9,10]. Considering the literature data [19–22], for both temperatures the “radiation induced hardening” regime should dominate. Available experimental data on radiation damage effects in beryllium are mostly collected from materials irradiated by fission reactor neutrons. However, the applicability of the data for fusion reactor applications and accelerator

driven particle sources is uncertain, since fission-spectrum neutrons do not induce sufficient levels of transmutation-produced helium [11–13]. In the current work, an ion beam accelerator was used to introduce radiation damage and about 2000 appm He, relevant to both fusion and accelerator applications and giving also the advantage of fast and relatively inexpensive materials irradiation without activating the sample.

Nanoindentation is widely used for evaluation of local mechanical behaviour of materials at micro-scale and is particularly useful for ion irradiated materials where only a shallow damaged layer is available. It has been successfully used for screening of radiation induced hardening in different nuclear materials, including: ferritic-martensitic [27–29], austenitic [30] and RPV [31] steels, ODS alloys [32] and tungsten [33,34]. No nanoindentation data on radiation hardening of beryllium is available in the literature; however the applicability of the technique to examine the effects of impurities on the hardness of beryllium was recently demonstrated [35].

Micro and macro-hardness examinations of beryllium often show significant scatter of indentation results [35,36] that may complicate the determination of radiation-induced hardening effects. This originates from the high elastic and plastic anisotropy of beryllium [25,37]: the room temperature (RT) critical resolved shear stresses for <*a*> basal slip (the primary slip system at RT) is 15 MPa, for the <*a*> prismatic systems is 68 MPa and the secondary <*c* + *a*> pyramidal systems is *2000* MPa [37,38]. Previous experiments [35,39,40] showed that indentation hardness coupled with crystallographic data from EBSD or XRD is a useful approach for comparing the effects of different treatments on beryllium. This approach is used here, with special attention being paid to the mitigation of any artefacts originating from localised plastic deformation of the surface around the indents (so-called pile-ups and sink-ins) which can significantly affect interpretation of nanoindentation data in beryllium [35].

The paper is structured as follows. First, the investigated beryllium grades, irradiation conditions, the nanoindentation hardness experiments and data treatment approaches are described. Then, the microstructure of the implanted layers are shown and discussed. Before hardness values are calculated,

indentation contact areas for different samples and different crystallographic orientation of grains are analysed, taking into account any pile-up and/or sink-in, and the tip-indented surface contact area coefficients are reported. The resulting correction parameters are then used to calculate the nanoindentation hardness of beryllium grains of different purity and different crystallography before and after irradiation. After, the load - indentation depth curves from different beryllium states (material grade, irradiation condition) are presented and the pop-in events (horizontal plateaux observed on the load-displacement at some at some critical loads) are characterised to highlight differences between different states of the materials. This is followed by a general discussion of the origins of the observed irradiation induced hardening and the applicability and significance of the obtained data for engineering design considerations for nuclear facilities with beryllium elements under irradiation.

2. Materials and techniques

2.1 Materials

Two vacuum-hot-pressed industrial beryllium grades were investigated in this work: a high purity nuclear grade S-65 (Be > 99.2%) [41] and the lower purity structural grade S-200-F (Be > 98.5%) [42]. Microstructures of both types are reported in Ref. [35]. The grades have similar average grain diameters of 7.2± 4.4 μm [35]. Our previous STEM/EDS studies of beryllium [18] showed that grain boundaries of both grades are decorated by numerous precipitates enriched by oxygen, aluminium, iron, silicon, magnesium, titanium and other impurities, while the grain cores are mainly free of precipitates.

2.2. Irradiation conditions

Before helium implantation, surfaces of samples were mechanically ground and polished with SiC paper, diamond paste and finally colloidal silica. To avoid sputtering of beryllium during implantation, a 1 μm layer of aluminium was deposited by sputter coating at the surface of samples. The aluminium layer was removed after implantation by polishing in colloidal silica.

Implantation was done at the National Ion Beam Centre (NIBC) at the University of Surrey. Sequential irradiation with He^+ ions with eleven energies from 1.2 MeV down to 0.2 MeV with steps of 0.2 MeV was used to create approximately a 3 µm deep damaged layer, as calculated with SRIM (Stopping and Range of Ions in Matter) [43,44]. Totally, 8.8×10^{20} (He)atoms/m^2 were implanted. The radiation dose calculation was done using a displacement threshold energy of 31eV [45] and the ‘‘Quick’’ Kinchin and Pease option. The calculated average damage is 0.1 dpa with an average dose rate of 1.7×10^{-4} dpa/s. The average helium content in the damaged layer is 2000 appm; however there are wide oscillations around the average value (see Figure 1).

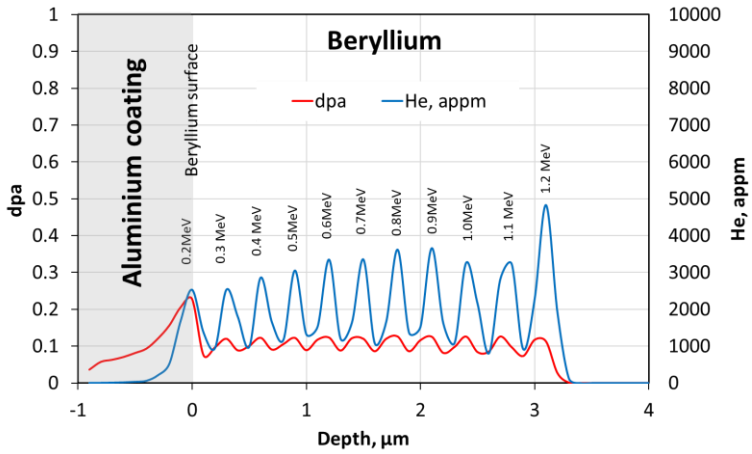

Figure 1. Helium implantation profile. 11 energies were used in the range from 0.2 to 1.2 MeV. The position of the Bragg peaks is marked with the corresponding implantation energy. The sample was coated by aluminium during implantation. The coating was removed before further analysis.

2.3.Experimental techniques

Indentations were conducted using a Keysight G200 nanoindentation system, with a diamond pyramid Berkovich tip, using the continuous stiffness measurement (CSM) technique [46] with a 42 Hz and 2 nm oscillation. The frame stiffness of the instrument and indenter tip was calibrated using a fused silica sample. An atomic force microscope Dimension D3100 was used for topographical investigation of the prints after indentation. The surface profiles were then obtained using the open source software Gwyddion [47]. These profiles were used to calculate the contact area between the indenter tip and the sample surface.

The nanoindentation hardness was calculated as

$$H = P/A \quad (1)$$

where A is the projected contact area between indenter tip and the sample at load P [48]. Two approaches were used for quantification of the contact area A: i) the method proposed by Oliver and Pharr [46] which forms the basis of the indentation testing standard [48] and ii) the method which uses the actual tip-surface contact area, corrected for effects due to pile-ups and/or sink-ins [49]. In the standard method proposed by Oliver and Pharr [46] the contact area is determined from the tip area function $A(h_c)$ that expresses the indenter's cross-sectional area in terms of the contact depth, h_c. The contact depth, $h_c = h_{max} - h_s$, is the difference between the measured total penetration of the tip into the surface, h_{max}, and the elastic surface displacement, h_s . The elastic displacement is calculated using the Oliver-Pharr model [46]: $h_s = \varepsilon \frac{P_{max}}{S}$, where P_{max} is the measured maximum load, S is the contact stiffness, which is computed as the slope of the unloading curve continuously evaluated in the CSM mode, and ε is the tip geometry coefficient (0.75 for a Berkovich tip) [50].

In the second method, the standard Oliver-Pharr algorithm for contact area calculation was modified in order to take into account the influence of the plastic deformation on the sample surface around indents during loading. The method is based on the approach proposed by Kese [49] and modified to include sink-ins effects [35]. The method requires experimental measurement of the indent profile through the central point of indentation and the centre of each edge. Where pile-up is observed, the contact between the indent and the pile-up is determined and is then projected onto the direction of the free surface normal, giving the pile-up height. The contact area of each pile-up is then approximated as a semi-ellipse, with the major axis equal to the length of the side of the projected triangular area of the indent print, and the minor axis being measured on the indent profile image as the projected distance of the pile-up contact perimeter [49]. Similarly, to account for sink-ins, the reduction in contact area was also approximated as a semi-ellipse, with a major axis calculated in the same way, whereas the minor axis was measured on the indent profile image as the projected distance

between the sink-in contact perimeter [35]. For the investigated indents the corrected projected area, A_{corr}, was calculated as the contact area determined by the Oliver–Pharr analysis [46], $A_{\mathrm{O-P}}$ plus (or minus) the area due to out-of-plane deformation near each edge for pile-ups (or sink-ins). In this paper $H_{O\text{-}P}$ refers to hardness values obtained with the Oliver-Pharr algorithm, whereas H_C refers to hardness values obtained after the contact area correction.

At least 200 indents were made for each sample with a target maximum indentation depth of 400 nm. Surface position correction was made for each indentation before data analysis. For consistency, load data averaged between 320 and 360 nm indentation depth were used for indentation hardness calculations, avoiding the depth range within which there is a strong indentation size effect [27,50]. Crystal Plasticity FEM calculations for beryllium [35] predict that the plastic zone beneath indents extends to a depth ~7× larger than the Berkovich tip penetration depth. The selected penetration depth for hardness calculations is almost 10 times smaller than the thickness of the implanted layer, allowing minimisation of any possible influence of the non-irradiated substrate material on the radiation-induced hardening data.

Because of the high hardness anisotropy of beryllium [35], in this paper indentation data are presented and discussed according to the angle between the indentation direction and the [0001] axis of the indented grain, denoted as θ. To investigate the crystallographic dependence of nanoindentation hardness, EBSD analyses of the indentation arrays were made, using a JEOL 840A scanning electron microscope equipped with the EDAX-TSL EBSD; OIM TSL software [51] was used for analysis of the EBSD data. Indents on or near to grain boundaries (no more than 2μm away) were not considered in analysis.

To investigate residual strains in samples after implantation and possible effects on nanoindentation data, a confocal Raman imaging microscope (WITec alpha300 AR) has been used to acquire Raman spectra and perform large area scans (3 mm × 3 mm). The analysis is based on determining the peak-shift corresponding to a E_{2g} stretching band [52] in beryllium. The peak shift is

caused by small changes to the short-range order in the atomic arrangement of the implanted material. Therefore, it is indicative to the micro-strains created by implantation. During the experiments firstly, the structural and strains heterogeneity evidenced by a change in the spectral pattern have been determined, and then the main spectral components in homogeneous regions have been calculated. Thus, by accumulating a large number of pixels ($600 \times 600 = 0.36 \times 10^6$), the position measurement error of the beryllium main peak is greatly reduced for the averaged spectral components. The TrueSurface feature enabled dynamic focusing of the confocal laser during scanning. Data acquisition was carried out with the conventional charge-coupled device (CCD) camera in the low-noise high-intensity detection mode with a dwell time of 0.5 s per pixel using a green laser ($\lambda = 531.95$ nm with an estimated penetration depth of about 30 nm [52]), a 1800 g/mm grating and a Zeiss EC Epiplan-Neofluar 50× long-distance objective to accommodate for topography variation during scans. The laser power was set at 15 mW. The system was pre-calibrated to maximise the intensity of the silicon main peak on a single crystal silicon reference sample. Resulting spectra were treated with a cosmic-ray removal procedure and a shape-based background subtraction algorithm in WITec Project FIVE 5.2 Plus post-processing software. Where applicable, a Lorentzian function was used for peak fitting of the background-subtracted data.

Samples for Transmission Electron Microscopy (TEM) were prepared by Focussed Ion Beam sectioning (FEI Helios NanoLab 600i). The 30keV Ga^+ ions have been used for lamellae lift-out and shaping and 5keV Ga^+ ions have been used for final thinning of lamellae. According to SRIM calculation, the final energy should create approximately 10 nm deep surface damaged layers and as it will be shown later, this greatly hindered displacement damage effect from helium ions implantation.

Observation of the irradiated layer was performed with the JEOL JEM-2100 TEM in the Materials Department of the University of Oxford.

3. Experimental results

3.1. Microstructure of the implanted layer

The implanted layer was investigated by TEM. On bright-field images radiation damage appeared in the form of “black dots” (less than 10 nm diameter) arranged in lines parallel to the surface of samples, as shown in Figure 2 for the S-65 sample irradiated at 50°C. Figure 2(a) shows that the dark lines correspond to the peaks in “dpa” and helium implantation (Figure 1), with energies from 1.2 MeV located in the lower right corner and nine lower energies down to 0.3 MeV in the upper left corner near the lift-out edge (see the simulated implantation profile in Figure 1). These “black dots” are likely to correspond to small dislocation loops or point defect clusters. While the dark areas correspond to approximately 1.2 dpa and 3000 appm of helium, the relatively bright areas in the implanted layer have approximately 0.8 dpa and 1000 appm of helium. The thickness of the dark lines is about 150 nm, separated by similar thickness bright areas with smaller number of defects (Figure 2(b)). Note that the displacement damage peaks should be 50 to 100 nm closer to the surface than the helium peaks, but this was not resolved by TEM as there is no clear substructure of the dark bands. Comparison with the microstructure below the 1.2 MeV implantation Bragg peak, where only FIB damage is present, shows that gallium damage of the TEM samples during preparation by FIB creates similar “black dots” in beryllium, so it was difficult to make accurate quantitative analysis of the initial radiation exposure. Assuming homogeneous distribution of FIB induced loops and after subtraction of this background, the estimated number density of loops was between $4\times10^{21}m^{-3}$ and $1\times10^{22}m^{-3}$ inside bright bands and between $2\times10^{22}m^{-3}$ and $5\times10^{22}\ m^{-3}$ inside dark bands. The damaged layers of the samples exposed at 50 and 200°C appeared very similar and no difference in substructure of the irradiated layers was noticed between two investigated beryllium grades. However, any differences could be being masked by FIB damage.

It should be also noted that in Figure 2, only 10 out of 11 implanted layers are present since the first layer was polished-off during colloidal silica polishing of the aluminium coating after the implantation, but, as will be discussed later, this was not the case for all the implanted samples.

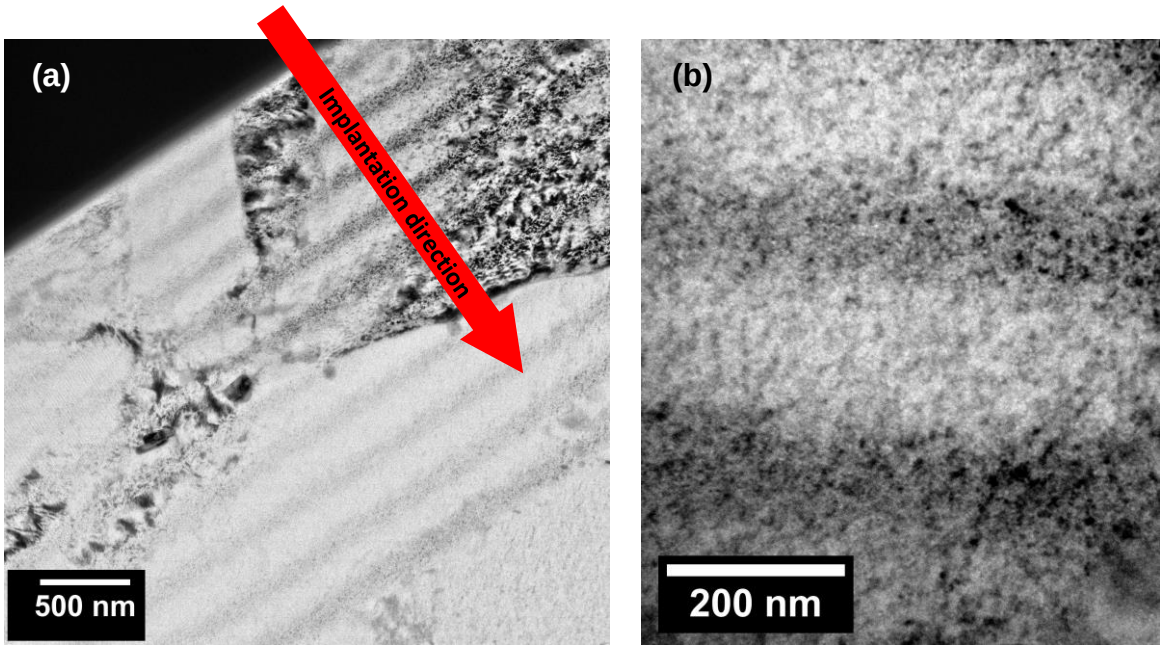

Figure 2. TEM image (bright field) of the S-65 irradiated at 50°C. The dark lines in (a) correspond to the peaks in "dpa" and helium implantation. Radiation damage appeared in the form of "black dots" with higher number density inside dark lines (b).

Use of over-/under-focus imaging [53] did not reveal any objects which could be identified as cavities or helium bubbles in any of the investigated samples, including in grain boundary areas. Helium is therefore likely to be either in solid solution in the beryllium matrix or in a form of sub-nanometric bubbles too small to be resolved in TEM [53]. The observation are in agreement with other experimental studies of beryllium after neutron irradiation [11,20,54–56] or helium implantation [24] where, due to the low diffusive mobility of separate helium atoms or helium-based complexes, gas bubbles were not visible in TEM at temperatures below 400°C. It is also known that at very high helium contents (> 25000 appm) helium bubbles may be observed even at low temperatures in neutron irradiated [57] or helium implanted samples [58], but this level is well above the helium concentrations investigated in this work.

3.2. Topography of indentation prints and contact area correction

The elastic, plastic and strain-hardening properties of a material can affect whether material will either plastically sink-in or pile-up around the indenter [50,59,60]; such topographical changes can significantly change the contact area between the indenter tip and surface. This deformation is not accounted for in the standard method of contact area determination proposed by Oliver and Pharr [46], so with this method the calculated indentation hardness would be too high if pile-up occurs (as the real contact area is greater than that calculated from the indenter profile and penetration depth) and too low when sink-in occurs (when the real contact area will be less than the calculated one). To estimate the out-of-plane plastic deformation of beryllium and hence to improve the analysis of the load-displacement data to give a true value of indentation hardness, direct imaging of the residual impressions was performed. Between 15 and 19 topography maps of indentation prints were made with AFM for each irradiated sample to cover the full range of indentation orientations for every investigated sample. Mapping was performed for the indents where the crystallographic orientation of the indented areas was confidently known (i.e. inside grains).

Figure 3 shows examples of topography maps around indents into differently oriented grains in irradiated and non-irradiated samples. In the majority of indents plastically deformed surface zones were observed well outside the area of the final tip penetration. Figure 4 shows changes in contact area between the indenter and the sample due to pile-ups and sink-ins, as a function of indentation angle, as a contact area correction coefficient, C, defined as:

$$C = \frac{A_{\mathrm{corr}} - A_{\mathrm{O-P}}}{A_{\mathrm{O-P}}} \qquad (2)$$

Here, A_{corr} is the measured projected contact area and $A_{\mathrm{O\text{-}P}}$ is the "ideal" contact area calculated from the indenter penetration using the Oliver-Pharr method.

The effects of pile-ups and sink-ins in non-irradiated beryllium have been reported by us previously [35]. It was shown that the pile-up / sink-in behaviour depends highly on the crystallographic orientation of the indented grain. For indentations into grains with surface normal close to [0001] ($\theta < 15°$) (hard orientations) sink-ins were predominant, as shown by the yellow

“halo” around the indenter print in Figure 3(a). The corresponding correction coefficient *C* was measured to be in the range of approximately -0.1 to -0.2. Indentation into grains with higher θ produced both sink-ins and pile-ups, appearing as hills with height up to 250 nm on opposite sides of the indentation pit (see Figure 3(c-d)). The contribution of pile-ups in determining the real contact area increased with θ, and so the correction coefficient *C* gradually increases with indentation angle, reaching +0.25 for indents into grains with surface normal orientated perpendicular to [0001]. This variation of C with grain / indenter orientation for unirradiated Be is indicated by the shaded area in Figure 4.

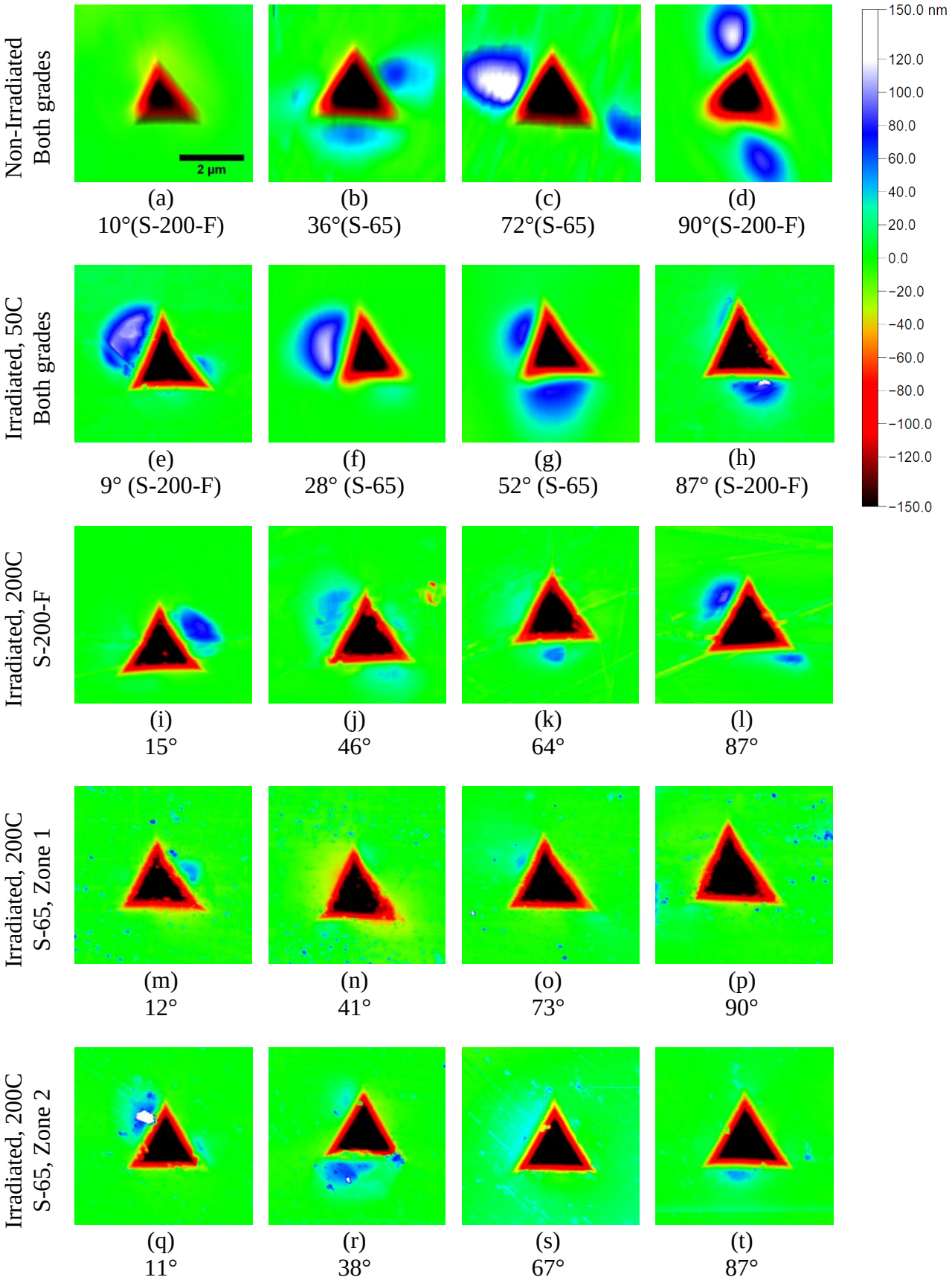

Figure 3. Examples of topography maps of 400 nm indents for S-65 and S-200-F grade in the as-received condition and after He implantation at 50°C and 200°C

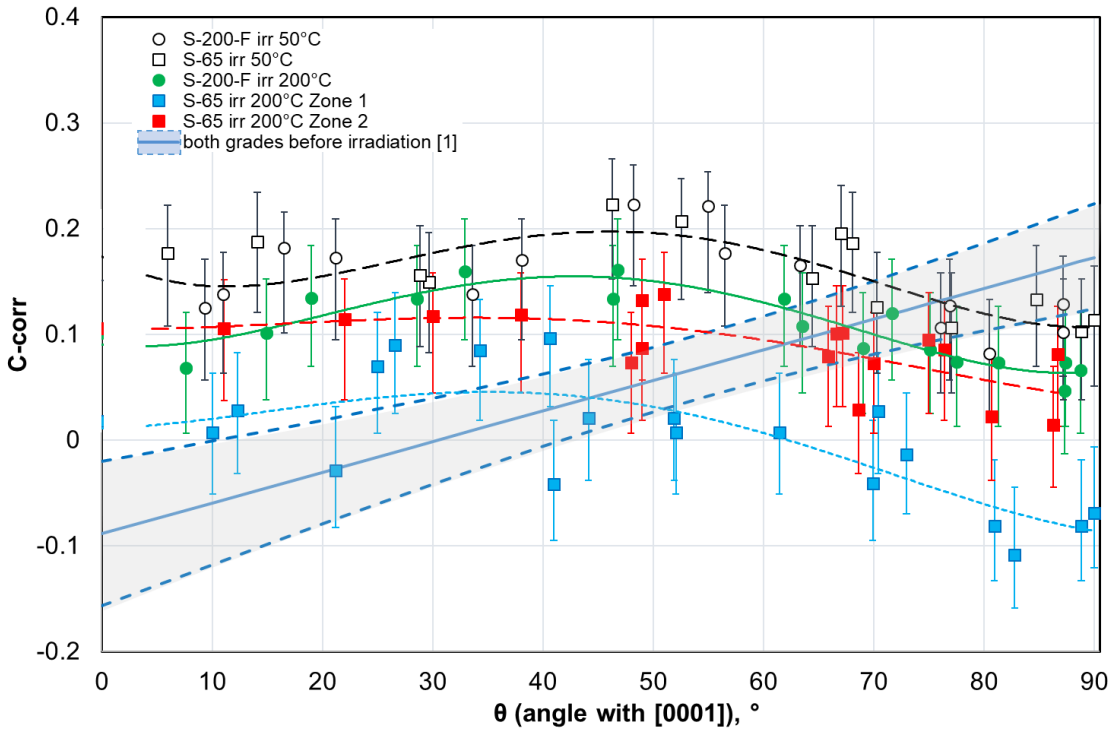

Figure 4. Distributions of the contact area correction coefficient for different crystal orientations in as-received conditions [35] and after irradiation at 50 and 200°C . Error bars in the implanted samples data points – min and max values considering 30 nm uncertainty of the contact area edge determination. Gray area is the 95% confidence interval for the non-irradiated samples

.

Pile-up behaviour was very different in the irradiated samples of both materials types. After irradiation at 50ºC, pile-ups dominated in all the mapped indents for all the crystallographic orientations of the indented grains as shown in Figure 3(i - l) and no significant difference in behaviour of the two investigated grades was noticed. The corresponding average correction coefficients (black open markers in Figure 4.) were around +0.15 for θ up to 30°, increasing slightly to a maximum of about +0.2 for θ between 40° and 60°, and decreasing to +0.1 for θ close to 90°.

Similarly, pile-ups dominated in the indents in the S-200-F grade irradiated at 200°C (Figure 3(e - h)), but the overall contribution into the contact area was smaller with an average correction coefficient of about +0.1 for small θ, a maximum of +0.15 for θ between 40° and 60° and a minimum of +0.07 for θ close to 90°.

The S-65 sample irradiated at 200ºC showed more complicated behaviour: in the area initially studied (Figure 3(e - h)), denoted as "Zone 1", sink-ins (Figure 3(e - h)), rather than pile-ups, dominated the material's indentation behaviour and correction of contact area. Because of this discrepancy, a smaller array of 75 indents was made in a different area of the sample ("Zone 2"), in which, similarly to other irradiated samples, pile-ups dominated behaviour around the indents (Figure 3(e – h). As is shown by blue markers in Figure 4, in "Zone 1" of this sample the average correction coefficient *C* was near 0 for small θ, had local maximum of about +0.05 for θ between 30° and 40° and decreased to -0.1 for θ close to 90°. In the second area ("Zone 2" in Figure 4), the correction coefficient distribution was very similar to that observed for the S-200-F grade irradiated at the same temperature, with a somewhat lower local maximum in *C* of about +0.1 for θ between 30° and 60°. The selection of the area for the second array was based on study of post-irradiation microstructures and their dependence on sample preparation, and is discussed later in section 3.4.

3.3. Nanoindentation hardness

Hardness values for all of the investigated samples were calculated accounting for the contact area correction, using the measured pile-up and sink-in contribution coefficient C from Figure 4, combining equations (1) and (2):

$$H_c = \frac{H_{O-P}}{C+1} \qquad (3)$$

where H_{O-P} was extracted from the nanoindentation test data using the standard Oliver-Pharr method [46]. As was shows in our previous work [35], for unirradiated materials, the averaged correction coefficient as a function of indentation angle θ (in degrees) between the *c* axis of the grain and the loading direction can be fitted to a linear function:

$$C = a_1\theta + a_0 \qquad (4)$$

where coefficients a_1=0.0035 and a_0= −0.123 for the chosen indentation depth range [35]. To account for the more complex variation of *C* with orientation in the irradiated materials, a fourth degree polynomial function was used:

$$C = a_4\theta^4 + a_3\theta^3 + a_2\theta^2 + a_1\theta + a_0 \quad (5)$$

Best-fit values of the coefficients and the coefficients of determination R^2 are given in Table 1.

	Non irradiated S-65 and S-200-F (from [35])	**S-65 and S-200-F irradiated at 50ºC**	**S-200-F irradiated at 200ºC**	**S-65 irradiated at 200ºC**	
				Zone 1 (sink-ins)	Zone 2 (pile-ups)
a_4		3.09×10^{-08}	2.5×10^{-08}	1.34×10^{-08}	6.21×10^{-09}
a_3		-6.02×10^{-06}	-4.45×10^{-06}	-2.32×10^{-06}	-1.14×10^{-06}
a_2		3.47×10^{-04}	2.08×10^{-04}	8.56×10^{-05}	4.66×10^{-05}
a_1	3.5×10^{-03}	-5.72×10^{-03}	-1.23×10^{-03}	2.48×10^{-04}	-2.05×10^{-04}
a_0	-1.23×10^{-01}	1.74×10^{-01}	9.06×10^{-01}	1.13×10^{-02}	1.05×10^{-01}
R^2	0.72	0.60	0.83	0.61	0.45

Table 1. Fitting coefficient (a_0 to a_4) and coefficients of determination R^2 for averaged correction coefficient as a function of indentation angle θ between the c axis of the grain and the loading direction for S-65 and S-200-F grades in as-received and irradiated states

Figure 5 shows the averaged nanoindentation hardness values for tests performed in grain interiors only in as-received and implanted samples and compares values before and after contact area corrections. The numeric values describing the observed trends are summarized in Table 2. The S-200-F has about 8% higher average hardness than the S-65 grade in as-received state and remained harder after helium implantations. The implantation at 50ºC almost doubled the hardness and the irradiation induced hardening of the lower-purity grade was about 10% higher. The irradiation at 200ºC led to 60% increase average hardness for both grades. The contact area correction led to about 10% decrease of the average hardness values and in general was slightly higher in the irradiated samples. It is important to note that while the average non-corrected hardness of the S-65 grade (200ºC irradiation) in Zone 1 and Zone 2 was different, the contact area corrected values were identical, highlighting the

importance of the nanoindentation artefacts mitigation for increasing accuracy of the experimental data.

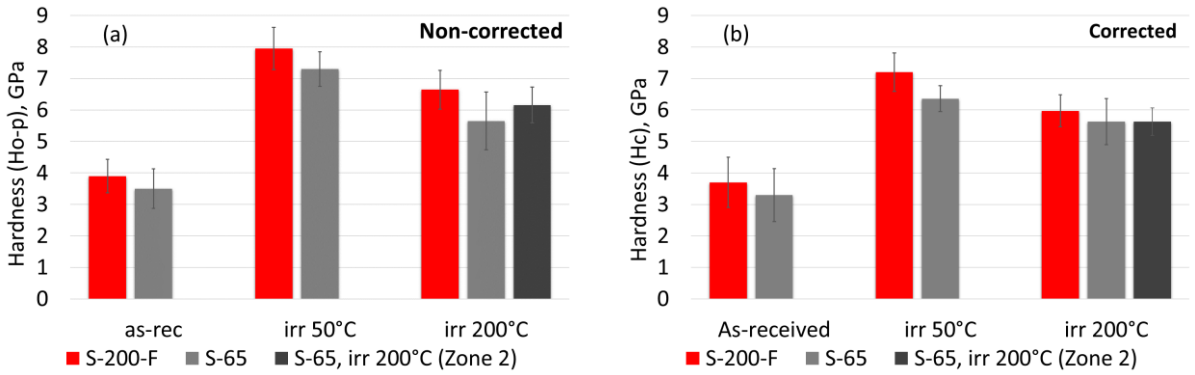

Figure 5. Average nanoindentation hardness from 2 beryllium grades before and after helium implantation ant 50 and 200ºC. (a) – contact area corrected values vs (b) – obtained by standard method.

Figure 6 shows the orientation dependence of nanoindentation, before and after the correction for surface topography. For all samples the curves have sigmoidal variation with indentation angle, with maximum and minimum hardness for indentation directions (test surface plane normals) parallel and perpendicular to [0001] respectively. Tsuya [40] and Hill and Jones [39] observed similar trends in micro- and macro-hardness tests of beryllium monocrystals.

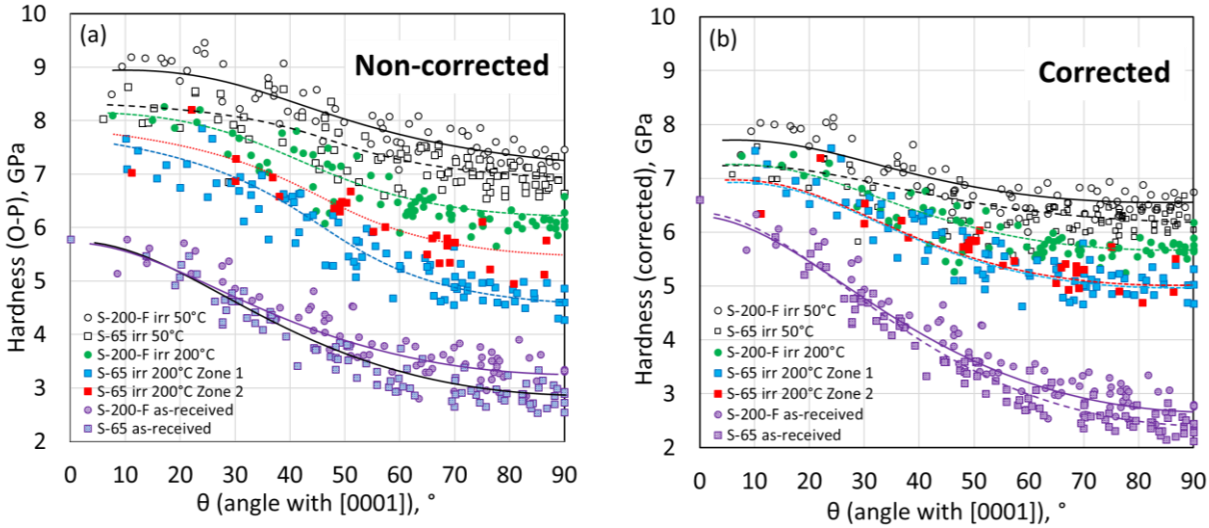

Figure 6. Nanoindentation hardness from 2 beryllium grades for different crystallographic orientation, calculated with the: (a) corrected via profilometry data using equations (4) and (3); (b) Oliver-Phar method [46]. 0° corresponds to indentation into the basal plane parallel to the [0001] direction, 90° implies indentation perpendicular to [0001]. Only data from grains with the

assigned crystallographic orientation are shown (no data from indents on or close to grain boundaries).

Figure 6 also compares area-corrected and O-P hardness distributions. In the non-irradiated samples, when corrected, the true hardness in "hard" orientations (θ close to 0°) is higher than the uncorrected value, due to sink-ins, whereas the true hardness in soft orientations (θ close to 90°) is lower than the uncorrected value, due to pile-up. Therefore, hardness values derived from the O-P method underestimate the hardness anisotropy. A different behaviour was observed in the irradiated samples. Since the pile-up / sink-in effects were less dependent on crystallography, the corrected hardness values were mainly simply shifted in magnitude from the O-P values, only slightly affecting the measured hardness anisotropy.

Before irradiation the lower purity S-200-F grade had slightly higher hardness for the same crystallographic orientations than the high purity grade S-65. This was especially noticeable for the "soft" orientations (see Table 2). Since only limited data were available for indentations close to [0001] and given the observed scatter, the "hard" grain hardness may not be accurately compared. Aldinger [25] found that the critical resolved shear stresses (CRSS) for both basal and prismatic slip in beryllium is proportional to the impurity concentration as $c^{2/3}$, (where c is the impurity concentration in wt%), so the less pure S-200-F would be expected to have increased in CRSS and thus higher hardness.

In both grades and for the both implantation temperatures the largest radiation hardening effect was observed in "soft" orientations perpendicular to [0001] (Figure 6). Starting from 2.5 GPa and 2.8 GP in as-received S-65 and S-200-F grades respectively, the hardness doubled after irradiation at 200°C and was 130-140% higher after irradiation at 50ºC, as demonstrated by black (for the S-65 grade) and red (S-200-F grade) data points in Figure 6(b). In absolute values the radiation induced hardening for the "soft" orientation after 50ºC irradiation in both grades was 3.7 GPa; and after 200ºC irradiation was 2.5 GPa for the S-65 and 2.9 GPa for the S-200-F. For the 200ºC irradiation, these changes are masked by considering only average hardness values, over all orientations (see Figure 5).

After the 50ºC irradiation, the average hardness of the S-200-F was higher than of the S-65, but the crystallographic analysis demonstrated that this was due to a larger number of grains with “hard” orientation being tested in the S-200-F. These effects demonstrate the importance of the use of crystallographic information in studies of the hardness of beryllium and other highly anisotropic materials. The “hard” orientation hardness values were less affected by radiation, therefore, implantation led to decrease of the anisotropy of beryllium hardness.

The high hardness anisotropy of beryllium originates from the very high anisotropy of the CRSS required for activation of different slip systems [35,39,40]. The CRSS is relatively low for the <*a*> basal and prismatic systems which both provide slip perpendicular to the c-axis, but it is very high for the secondary <*c* + *a*> pyramidal systems [37,38] responsible for deformation parallel to the *c*-axis, especially under compression [25]. Point defect clusters, helium-vacancy clusters (and potentially, sub-nanometric He bubbles) are likely to increase the CRSS values of all slip systems by roughly the same absolute amount, and so to decrease the relative differences between CRSS values of the slip systems. A similar effect was observed by Hill and Jones [39], who demonstrated that work hardening of beryllium single crystals led to highly non-uniform increases of Vickers hardness: about 350 MPa for basal plane indentations and about 660 MPa for indentations on prismatic planes.

	S-65						S-200-F					
	H_{O-P} [1]			H_C [2]			H_{O-P}			H_C		
	As-received [35]	He implanted		As-received	He implanted		As-received	He implanted		As-received	He implanted	
		at 50ºC	at 200ºC		at 50ºC	at 200ºC		at 50ºC	at 200ºC		at 50ºC	at 200ºC
Average hardness inside grains, GPa	3.5 ±0.6	7.3 ±0.5	5.6 ±0.9	3.3 ±0.8	6.4 ±0.4	5.6 ±0.7	3.9 ±0.5	8.0 ±0.7	6.6 ±0.5	3.7 ±0.8	7.2 ±0.6	6.0 ±0.5
Radiation hardening ΔH, GPa	-	3.8 ±0.8	2.1 ±1.1	-	3.1 ±0.9	2.3±1.1	-	4.1 ±0.9	2.7 ±0.8	-	3.5 ±1.0	2.3 ±0.9
Average hardness, GPa	3.7 ±0.6	7.4 ±0.6	5.6 ±0.8	-	-	-	4.1 ±0.5	8.0 ±0.7	6.6 ±0.6	-	-	-
H_{min} (⊥ to [0001]), GPa	2.8	6.9	4.6	2.5	6.15	5.1	2.8	7.3	6.0	2.8	6.6	5.7
H_{max} (‖ to [0001]), GPa	5.6	8.3	7.5	6.5	7.6	7.2	6.3	9.0	8.0	6.3	7.9	7.3
Minimum Be content [3], %	99.0						98.5					
Main impurities[3], appm	O=3260, C=680, Fe=130, Al=170, Si=145						O=5450, C=1150, Fe=210, Al=340, Si=193, Mg=130					

[1] Calculated using the standard Oliver-Pharr algorithm [46].

[2] Contact area corrected data using equation (3) which considers pile-up/sink-in contribution using the crystallographically dependent area correction coefficients calculated with equation (4).

[3] The nominal chemical compositions of the grades, which specify maximum content of different impurities, (Materion Electrofusion Corporation)

Table 2. Nanoindentation, microstructural and chemical composition data from two beryllium grades before and after helium implantation

3.5. Indentation pop-ins

Figure 7 shows examples of curves of indentation load as a function of depth for S-65 (unirradiated, and irradiated at 50ºC and 200ºC "Zone 2"); the behaviour of the S-200 grade material was very similar. Four curves at different indentation orientations are shown per state. The majority of the curves exhibit discrete displacement bursts, the so-called "pop-in" effect, at different stages of indentation, as highlighted by black arrows Figure 7. This pop-in behaviour has been widely observed in different materials [27,61–63]; in the early stages of indentation (< 50 nm indentation depth) pop-ins are typically associated with plasticity bursts caused by dislocation source nucleation in previously defect-free material [27,61–63]. In our experiments these early-stage pop-ins were observed in non-irradiated samples in both grades (Figure 7(b)), but were absent after helium implantation at both temperatures Figure 7(d, f). This could be explained by the high number density of defects (in our case point defect cluster, He-vacancy complexes or He bubbles) which can potentially serve as nuclei for dislocation sources; similar effects have been found in indentation of ion-irradiated Fe-Cr [27] and W [64] and polycrystalline Fe after plastic deformation [63].

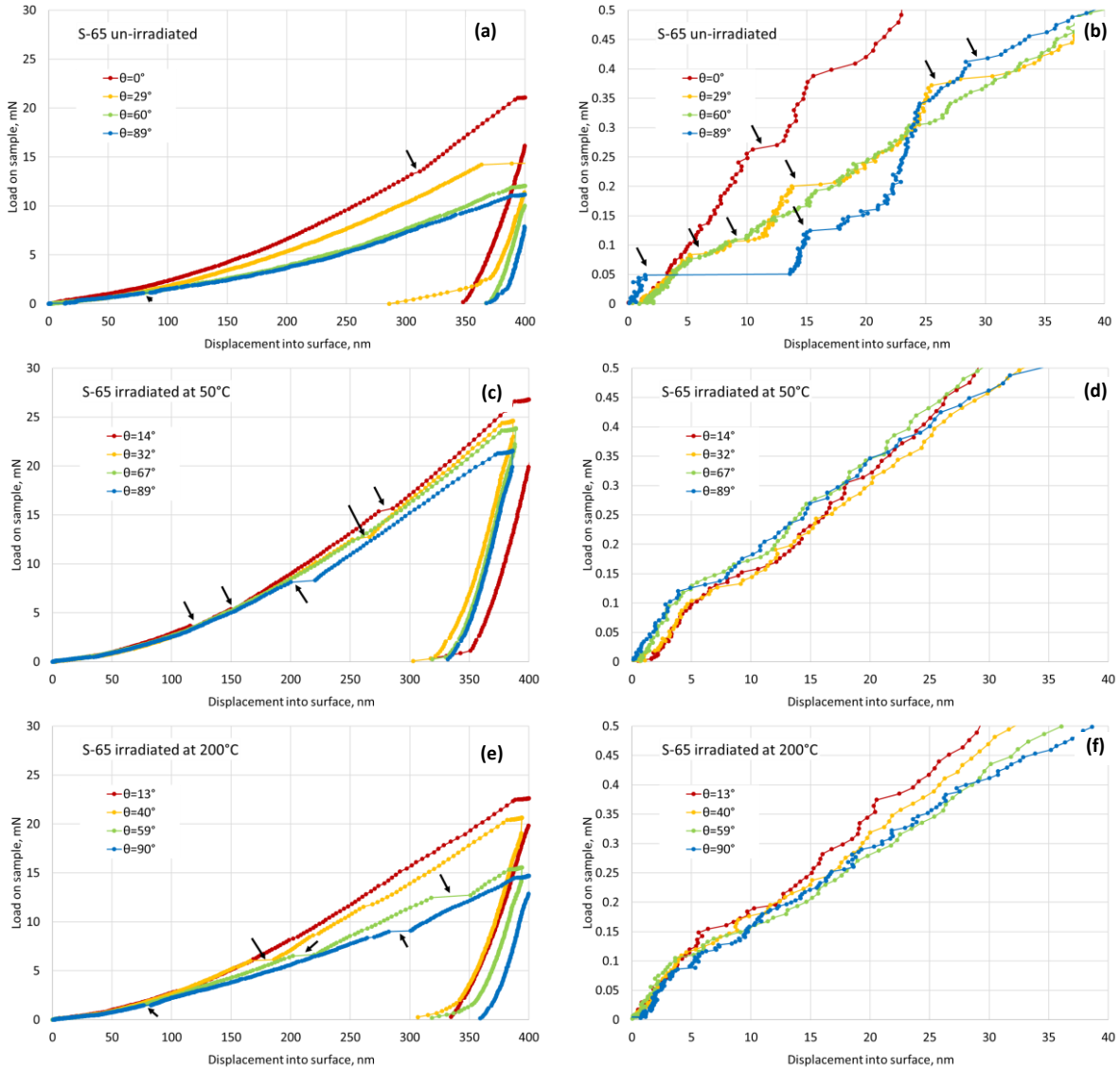

Figure 7. Typical load–indentation depth data produced from the as-received S-65 beryllium grade (a-b) and after helium implantation (c-f); black arrows indicate pop-in events. Curves in (b), (d) and (f) are initial stage fragments of curves in (a), (c) and (e) correspondently

Sometimes large pop-ins were observed at relatively high indentation depths (>100 nm); see Figure 7 (a, c, e,). This behaviour was strongly affected by the sample condition: while only about 7% of load displacement curves in as-received materials had any of these pop-ins, the behaviour was observed 3 to 6 times more often in helium-implanted samples. Such large pop-ins at relatively high indentation loads have also been observed in polycrystalline iron [63]; it was concluded that these events were closely related to the presence of a grain boundary in the stress zone of the indentation and has been rationalised in terms of preferred emission of

dislocations from the grain boundaries. Such grain-boundary related pop-ins have also been observed in Au/Si samples [62] and Fe-C alloy [65]. Our investigations in beryllium consider indentations made in grain centres as observed at the surface by EBSD. It is however, possible that the indentations are interacting with grain boundaries under the surface, invisible to SEM/EBSD, which might possibly introduce some pop-ins observed in beryllium in this work. However, in that case, the pop-in behaviour should be a statistical process dependent on presence of grain boundaries (i.e. grain size), and not be dependent on irradiation condition, since the grain size did not change during the implantations. Currently this behaviour is not understood. It is possible to propose that the substructure of the implanted layer with sequence of “softer” and “harder” bands can cause avalanche-like deformation when the stress zone reaches deeper “soft” layers.

3.4.Investigating the complex behaviour of S-65

It was observed that irradiation highly affected pile-up/sink-in behavior of beryllium: it become less crystallographically dependent with increased domination of pile-up (see Figure 3 and Figure 4). However, the S-65 sample irradiated at 200ºC have more complicated behaviour: in one area (denoted as "Zone 1"), sink-ins were mainly observed, while in a second area of the sample ("Zone 2"), similarly to other irradiated samples, pile-ups dominated. For better understanding of the behaviour, several TEM lift-outs were made from the indents in the S-65 and S-200-F grades irradiated at both temperatures. Results for the 200ºC irradiations are shown in Figure 8. The surface layers of the samples are different, due to differences in the degree of polishing away of the aluminium layer after irradiation but before indentation. In the S-65 grade sample (200°C implantation, "Zone 1" indentations) (Figure 8a) , the surface is in the middle of the dark line with an increased number density of black dots (and, from Figure 1, high helium content) while in lift-outs from other sample (S-200) the surface layer was inside the bright band with fewer point defect clusters (and lower He content). Note that the S-65 sample irradiated at 50°C had the bright near-surface layer was (Figure 2a).

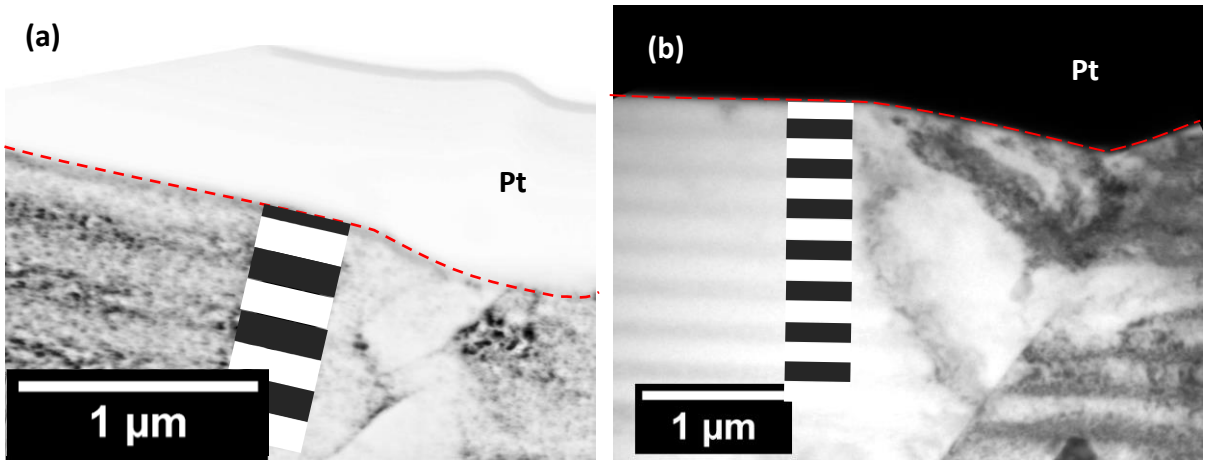

Figure 8. TEM images of the (a) S-65 irradiated at 200ºC (inverted colour dark filed image) and (b) S-200-F, irradiated at 200°C (bright field image) taken near the indenter prints. The sequence of the dark and bright layers is highlighted by black and white lines. The near-surface layer is "black" in the S-65 sample, and it is "white" in the S-200 sample.

This may be the origin of the observed differences in pile-up/sink-in behaviour after 200°C irradiation. It is known that pile-up / sink-in can be more pronounced for indentations in materials with a thin coating of different mechanical behaviour to the underlying substrate [50]. For indentation into hard coatings on a soft substrate promotes surface sinking-in, as observed by Tayebi et al during indentation of SiO_2 films on Al substrate [66], whereas for indentation in a soft coating on a hard substrate promotes surface pile-ups, as, for example, was demonstrated in the aluminium-on-glass system by Tsui et al [67]. The behaviour will be more complicated in the case of the heterogeneous layered irradiated substructure of the implanted layer of the investigated samples: the dark bands with increased black dot number density are likely to be harder, and possibly with a lower work-hardening rate, than the relatively bright areas between them. However, the surface layer of the S-200-F after 200°C irradiation shown in Figure 8b (and the other irradiated samples, which had a similar surface layer) should be softer than the material under it, corresponding to the "soft coating on the hard substrate" scenario (promoting pile-up), while for the S-65 "Zone 1" 200ºC irradiation shown in Figure 8a, corresponds to the converse "hard coating on the soft substrate", promoting sink-in, as observed. However, it is difficult to make a definitive conclusion on this, since only a few lift-outs were prepared and analysed with TEM from these samples.

To further investigate this assumption, Raman spectroscopy analysis was performed on both materials in the as-received state and after implantation at temperatures of 50ºC and 200ºC. A high-frequency acoustic mode is characteristic to beryllium, which results in a highly intense Raman peak (stretching band) [52,68]. Figure 9 shows the Raman spectra of Be samples in as-received state and after helium implantation. A single band was observed in both cases, which suggests the absence of a parasitic signal from impurities, e.g. oxygen. This band is initially positioned at 458.5 ± 0.1 cm^{-1} in the as-received samples. Both samples implanted at a temperature of 50ºC have shown a shift in the band position of -1.4 cm^{-1} in the S-200-F

grade and -1.5 cm^{-1} in the S-65 grade, while the corresponding shift in the same grades implanted at 200ºC was -0.5 cm^{-1} and -0.8 cm^{-1}. As a general rule, a shift in the position of the stretching band indicates a change to the local vibration modes, resulting in a slightly different short-range order of the beryllium atoms. Shifts similar in direction and magnitude have been observed in deuterium-implanted beryllium [52]. According to [69] downshifts of the stretching band can be attributed to a tensile stress in the material, that can be due to defects or impurities changing the bond lengths. Therefore, it is possible to assume that the surface tensile stresses exist in the irradiated samples studied here, but at a higher level in the samples irradiated at 50ºC than at 200ºC. The position the beryllium stretching band have been previously correlated with the hydrostatic pressure in diamond-anvil compression experiments [68], where a large positive shift was observed: an empirical ration between the observed Raman shift E (in cm^{-1}) and the applied pressure P (in GPa) was derived as: $E = 459 + 2.086P - 0.011P^2$. Using this equation, the estimated tensile surface stresses in the samples irradiated at 50°C are 500 to 540 MPa and 180 to 280 GPa in the samples after 200°C implantation. Note, that since the nature of the pressure in our samples differs from the compression experiments reported in [68], further numeric modelling is required to quantify and confirm the level of stresses is samples due to the helium implantation .

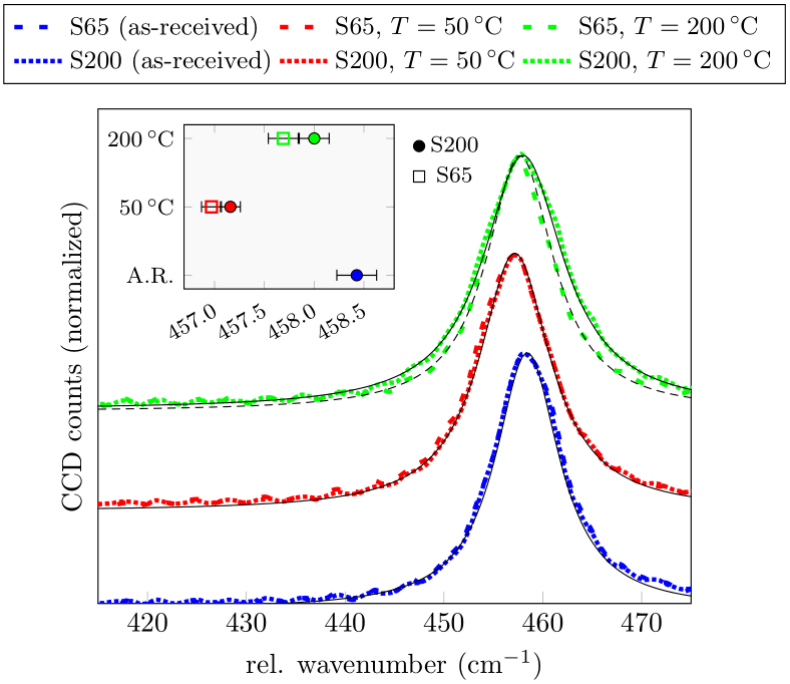

Figure 9. Raman spectra from two grades of beryllium (S-65 and S-200-F) in the as-received (A.R.) state and after helium implantation at 50 °C and 200 °C. Each spectrum was acquired by averaging over 0.36 × 10^6 individual spectra from 3 mm × 3 mm surface regions, thus reducing the noise originating from near-surface defects. The inset shows the peak positions, determined by fitting a Lorentzian function to the 420-490 cm^{-1} spectral region for each spectrum. The error bars reflect a systematic error introduced by the choice of the fitting function.

In contrast to other investigated samples where the beryllium stretching band position had not experienced spatial variation, the shift in the S-65/200ºC irradiation specimen had a distinct striped substructure consisting of regions with average band shift of about -0.6 cm^{-1} (yellowish areas in 10(a)) and regions with average band shift of -1.2 cm^{-1} (brownish areas in 10(a)). This substructure suggests varying surface tensile stresses which are likely to correspond to the alternation of surface-breaking layers of high defect density and low defect density. This could have been caused by polishing-removal of the aluminium layer being at a shallow angle to the initial surface plane, as schematically shown in Figure 10(b). The "Zone 1" indentation array in the S-65 sample implanted at 200ºC was located in the "brownish" band in Figure 10(a) with a high defect density, as seen by TEM in Figure 8(a). As discussed earlier, this corresponds to the "hard coating on soft substrate" scenario favouring the observed sink-

ins. The “Zone 2” array was made in the “yellowish” area in Figure 10(a) corresponding to the “soft coating on hard substrate” scenario favouring the observed pile-ups. For S-65 “Zone 2”, the downshift is almost equal to that for the S-200-F grade irradiated at the same temperature, as are the pile-up behaviour and the corresponding area correction function *C*. This supports our assumption that in the S-65 sample after 200ºC irradiation that the contrasted pile-up/sink-ins behaviours are due to the surface preparation of the sample and that in the implanted samples evolution of the pile-up behaviours (at least for the 200 ºC irradiation) is highly sensitive to the homogeneity and structure of the implanted layer. It should be noted that separate, more controlled experiment with implantation to different depths (at surface and below surface), without protective layers and preferably with broader Bragg peaks (as for example W self-ion implantation) should be performed to elucidate further the role of the damaged layer substructure on the pile-up/sink-in behaviours.

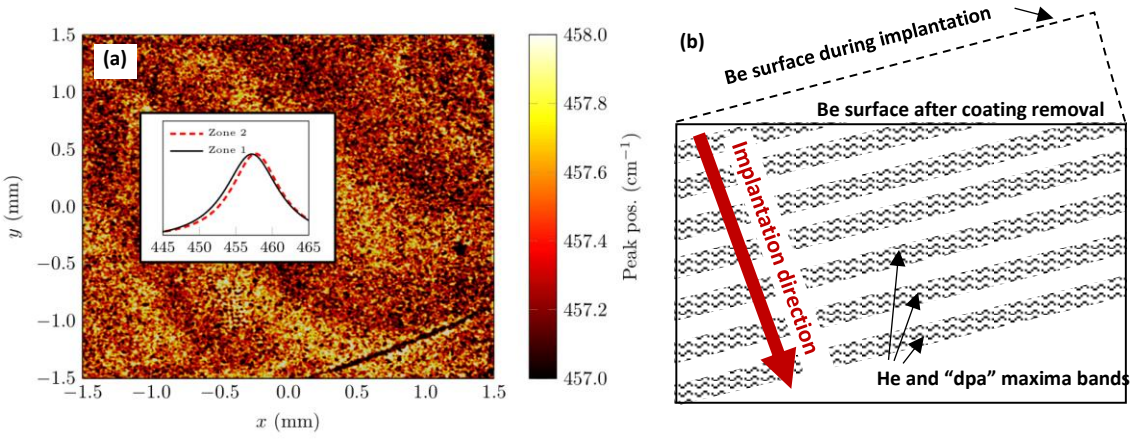

Figure 10. (a) Raman peak shift in the S-65 beryllium grade sample after irradiation at 200 °C, shown by applying a centre-of-mass filter to the background-subtracted spectra from a large area scan. Averaged Raman spectra corresponding to the high and low-wavenumber regions are plotted in the inset as (Zone 1) and (Zone 2) respectively. (b) schematic representation of the possible origin of the non-homogeneous Raman peak shift is the polishing of the sample after implantation at shallow angle to the initially implanted surface

4. Discussion

4.1.Pile up/ sink-in behaviour

In bulk materials it is generally observed that a high yield stress to elastic modulus (σ_y/E) ratio and a high strain-hardening rate both promote a spread of deformation deeper into the specimen and the surface around the indenter sinks-in; while the converse (low (σ_y/E) values and low strain hardening) favour localisation of deformation around the indents and the creation of pile-ups [50,59]. The pile-up/sink-in behaviour in anisotropic hcp metals like Be [35] or Ti [70] is highly sensitive to the crystallographic orientation of the indented grains. The observed crystallographic dependence of pile-up/sink-ins in non-irradiated beryllium is in good agreement with crystal plasticity finite element modelling (CPFEM) results [35], which demonstrated that the stress field and geometrically necessary dislocations (GND) penetrate deeper into the material in the "hard" orientation relative to the "soft" orientation, consistent with a higher (σ_y/E) ratio, also the plastic strain under the "hard" indent is also higher consistent with high GND hardening. Irradiation can induce hardening or softening, changing the (σ_y/E) ratio, and can change a material's strain hardening rate. Hence, as observed in this study and in other studies on different materials, the pile-up behaviour can be changed by irradiation. Similar to our observations, many studies report increased domination of pile-ups after irradiation. For example, Hardie et al [27] observed an increase in pile-ups heights after self-ion irradiation of iron-chromium alloys. Similarly, a substantial increase in pile-up heights was observed in a helium-implanted single crystal tungsten by Das et al. [71] and in tungsten-rhenium alloys by Beck et al [33]. However, in contrast, Armstrong et al. [72] observed a suppression of pile-ups in tungsten-tantalum alloys after self-ion implantation. It is clear that irradiation can change both the (σ_y/E) ratio and the strain hardening rate (through radiation induced hardening or softening), however the underlying mechanism of interaction of dislocations with radiation induced defects and implanted ions is not clear and is yet to be examined. Before a reliable model for prediction of pile-up behaviour is developed,

measurements of contribution of this artefact are highly desirable for accurate measurements of irradiation induced hardening.

4.2.Hardening

Although no obvious differences were noticed by TEM investigation between samples irradiated at 50°C and 200°C, that is highly likely the consequence of the FIB damage, the nanoindentation results demonstrated much higher hardening for the lower temperature irradiation. This is in agreement with other hardness and yield strength data of beryllium irradiated at different temperatures (see [24,73] and review [74]). For example, Snead [73] performed Vickers hardness measurements of the S65-C grade neutron irradiated in high flux beam reactor (HFBR) up to 0.34 dpa and 250 appm He and observed about 480MPa (converted from HV) hardness increase after irradiation at 95°C, about 335MPa increase for T_{irr}=205°C and about 265MPa increase for T_{irr}=278°C. These data was in good agreement with the yield strength increase which was 75 MPa, 55 MPa and 40 MPa correspondently [73]. Kesternich and Ullmaier [24] investigated tensile properties of high purity beryllium implanted by helium (220 appm, 0.02dpa) and observed 175 MPa increase in the yield strength after implantation at 100°C, which was about 90MPa after 300°C implantation.

Both helium and lattice defects introduced during the implantation are likely to act as obstacles to dislocation motion. While helium solubility in beryllium has not been measured, this inert gas generally has an extremely low solubility in metals [75]. Therefore, He is likely to be either trapped by vacancies, increasing the CRSS for dislocation movement by solid solution strengthening; or precipitated into sub-nanometric helium bubbles (too small to be resolved by our TEM), where a precipitation hardening mechanism will govern dislocation pinning and CRSS increase. Kesternich et al [24] investigated the influence of helium on yield strength of beryllium and concluded that for low temperature irradiation (100°C), even if

bubbles are not visible, the Orowan mechanism for dislocation pinning at precipitates (small bubbles) should be applied for description of radiation induced hardening. Kesternich et al [24] did not include hardening analysis from the observed dislocation loops.

The dispersed barrier hardening model was used to correlate the irradiation hardening and microstructure observed by TEM:

$$\Delta\sigma_y = \alpha M \mu b \sqrt{N \cdot d} \quad (6)$$

$$\Delta H = 3\Delta\sigma_y \quad (7)$$

where, $M = 4.3$ [76], $\mu = 132.8$ GPa [37,38] and $b = 0.228$ nm (<*a*> slip) [25] are the Taylor factor, shear modulus and Burgers vector, respectively, N is the number density and d is the mean diameter of obstacles (considered to be 5 nm for this estimation). α is the dimensionless obstacle strength factor in the range of $0 \leq \alpha \leq 1$. To estimate the possible hardening, as a guidance we used the α values of different types of defects summarised for steels by Lucas [77]: i) weak barriers like small bubbles, loops, vacancy clusters with $\alpha < 0.25$, ii) intermediate barriers such as Frank loops with $0.33 < \alpha < 0.45$, and iii) strong barriers such as voids and large precipitates with $\alpha \approx 1$ obstacles. Taking the average number density for the observed loops, the equations (6) and (7) yields $\Delta H \approx 0.85$GPa if $\alpha = 0.2$ (case of small loops is steels [77,78]) or , $\Delta H \approx 1.7$GPa if $\alpha = 0.4$ (case of Frank loops is steels [77,78]). Comparison with the radiation induced hardening data from Table 2 implies that that between about 1.4 and 2.4 GPa of hardness increase should originate from the other radiation induced obstacles, not observed by TEM and potentially related to helium. To analyse this, we considered two marginal scenarii: i) helium is homogeneously distributed in beryllium and cause solid solution hardening; ii) helium agglomerates and creates clusters with vacancies which act as barriers for dislocation movement.

In the case (i), it is possible to estimate the solid solution hardening using the equation proposed by Fleischer [79]:

$$\Delta\sigma_y = \frac{M}{760}\mu \cdot \delta^{\frac{3}{2}} \cdot c_{He}^{\frac{1}{2}} \qquad (8)$$

where, δ is a parameter characterising interaction between solute atoms and dislocations *and* $\cdot\, c_{He}$ is a concentration of helium atoms. With the Taylor factor $M = 4.3$ [76], shear modulus $\mu = 132.8$ GPa [37,38], $\delta = 1$ [24] and $\cdot\, c_{He} = 2 \times 10^{-3}$, equation (8) and (7) yield $\Delta H \approx 0.1 GPa$. This is one order of magnitude less than the anticipated contribution from helium; therefore, the observed hardening cannot be attributed to solid solution hardening by helium atoms.

The dispersed barrier hardening model (equation (6)) can be used to estimate hardening from helium bubbles. As no bubbles were observed by TEM we assumed that the hypothetical bubbles should have diameter less than 3 nm as this is the approximate size of the first bubbles observed in beryllium containing 2000 appm of helium during in-situ annealing inside TEM at 350°C [80]. Considering this size range, we estimated the corresponding number density of bubbles which can be created by 2000 appm of helium atoms. The approach was based on comparison of the expected pressure in bubbles depending on the properties of the materials (surface tension, shear modulus and Burgers vector) with the calculated pressure in bubbles of a specific size expected from the ratio between helium atoms and vacancies described by the equation of state. From one hand, assuming spherical bubbles, pressure (*P*) inside helium bubbles should be bound by the inequalities [81]:

$$\frac{2\gamma}{r_B} \leq P \leq \frac{2\gamma + \mu b}{r_B} \qquad (9)$$

where r_B is the radius of the bubble and $\gamma = 1.83\, J/m^2$is [82] the bubble surface tension, $\mu = 132.8$ GPa is the shear modulus [37,38], $b = 0.228$ nm is the Burgers vector [25]. The lower boundary is determined by the equilibrium pressure in a bubble of gas determined by Young–Laplace equation, and the upper boundary is determined by the loop-punching stress at which pressure in growing bubbles is relieved by "punching out" dislocation loops [81]. This

calculations show that the pressure in bubbles may vary from 2.3 GPa to 21 GPa for the bubbles with $r_B = 1.5nm$, and increases to the range from 14 GPa to more than 70 GPa for $r_B = 0.25nm$.

From another hand, the ratio between the pressure, quantity of helium atoms and size of a bubble (i.e. number of vacancies in the bubble) can be described by the equation of state. In this work we used the Benedict equation of state [83] parametrised by Mills, Liebenberg, and Bronson [84] as this approach demonstrated good results in predicting helium bubbles behaviour in tungsten [81]. The equation has a form of:

$$\frac{V}{n_{He}} = f_1(T)P^{-\frac{1}{3}} + f_2(T)P^{-\frac{2}{3}} + f_3(T)P^{-1} \qquad (10)$$

where V is a volume of a spherical bubble, n_{He} - number of helium atoms in a helium bubble, and $f_1(T)$, $f_2(T)$ and $f_3(T)$ are the functions dependent on the temperature, the details and parameters of which can be found in [84]. The volume of the bubble may be approximated as [81]:

$$V = n_V \Omega = \frac{4\pi r_B^3}{3} \qquad (11)$$

where $\Omega = 8.09 \times 10^3 nm^{-3}$ is the atomic volume of beryllium and n_V - number of vacancies in a bubble.

Combination of equations (9), (10) and (11) allowed estimation of the ranges of ratio between bubbles radii and quantity of helium atoms in the bubbles (Figure 11a). The range of about 1300 to 1660 He atoms per bubble is excepted for $r_B = 1.5nm$ ($n_V \approx 2000$), this decrease to $n_{He} \approx 400\ to\ 800$ for $r_B = 1.0nm$ ($n_V \approx 530$) and $n_{He} \approx 60\ to\ 125$ for $r_B = 1.0nm$ ($n_V \approx 65$). The presented numbers were calculated for the room temperature (RT) and there was only a little difference (<6% for the average n_{He} values) between data at RT, 50°C and 200°C. The average quantity of helium atoms per bubble as a function of quantity of vacancies (bubbles size) can be estimated by the generated equation: $n_{He} = 2.8 n_V^{0.87}$.

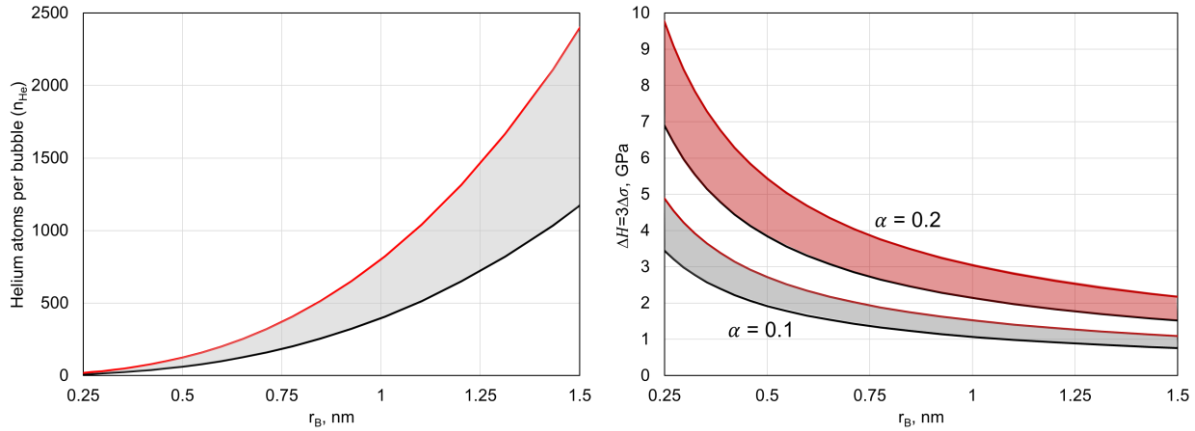

(a) (b)

Figure 11. (a) Correlation between quantity of helium atoms in the bubble and the size based on the Benedict equation of state; (b) calculated contribution of helium bubbles into the radiation hardening for different sizes and different obstacle strength factors.

Considering the implanted 2000 appm of helium and quantity of helium atoms per bubble of a specific size from Figure 11b, it is possible to estimate the range of the corresponding number densities of the bubbles: about 1.2×10^{23} and 1.9×10^{25} m^{-3} for bubbles with radii of 1.5 and 0.25 nm correspondently. The calculated number densities were used for estimation of the induced hardening (equations (6) and (7)). The results of the expected helium bubbles contribution into hardening ΔH are summarised by the ed area in Figure 11b for the case the obstacle strength factor $\alpha = 0.2$ (weak obstacles after Lucas [77]). As between 1.4 and 2.4 GPa is expected from these objects, it is possible to note that with the chosen calculation parameters, this corresponds to relatively large bubbles with the radius of 0.8 - 1.5nm. However, as demonstrated in [78], the strength factor of cavities is highly dependent on the size and for the case of stainless steel may decrees to the values of $\alpha = 0.02\ldots0.1$ if the cavities are smaller than 2 nm in diameter. The value of $\alpha = 0.1$ was also deduced for the helium bubbles with diameters of 1–1.5 nm in irradiated ferritic-martensitic steels [85]. The results of the expected helium bubbles contribution into hardening ΔH for $\alpha = 0.1$ are demonstrated by the grey area in Figure

11c, and the observed 1.4 and 2.4 GPa hardening will correspond to the helium bubbles with the radii in the range between about 0.4 and 1 nm.

Considering the obtained distribution of hardening for the bubbles of different sizes, it is possible to suggest that the differences between hardening at 50 and 200°C observed in our work could be explained by differences in spacing between the bubbles (i.e. number density of bubbles and their size), i.e. bubbles after 200°C implantation are larger than after the 50°C implantation, but still below the TEM resolution (1- 2 nm in diameter). It is also should be added that the ratio between vacancies and helium atoms may alter the bubbles strengthening factor α. For example, as it was shown by Schäublin and Chiu [86] in the case of bcc iron, a 2 nm He bubble is a weak obstacle when the He content is low, at 1 to 2 He atoms per vacancy, but beyond 2 He atoms per vacancy, the resistance of the He bubble increases with increasing He content (and pressure) and at 5 He atoms per vacancy, the He bubble becomes a much stronger obstacle. While, no detailed investigation of helium bubbles strengthening factors in beryllium is known, the scenario that increase of helium to vacancy ratio may increase strength factor of bubbles is likely. Due to this, it is possible to suggest that bubbles in the samples irradiated at 50°C may have higher H/V ratio (and potentially, higher strengthening factor) that the bubbles in the samples irradiated at 200C. This suggestion also complies with our Raman spectroscopy measurements. We observed that the samples after helium implantation at 50°C have higher surface tensile strains than the samples after 200°C implantation. Similarly, surface tensile strains have been observed synchrotron X-ray micro-diffraction by Hofmann et al. [87] in helium-implanted tungsten (RT, 3000 appm, 0.2 dpa). Using the relaxation volumes of defects derived from DFT, authors [87] demonstrated that the tensile strains were caused by self-interstitial atom defects which did not recombine with vacancies due to the presence of helium and creation of He_2V. The relaxation volumes of vacancies, interstitials and their complexes with helium in beryllium are unknown and require additional numerical modelling

investigation, however following the results in [87], it is possible to assume that the SIA have positive relaxation volume (relaxed volume of the supercell containing SIA is larger than the volume of the perfect cell), vacancies have negative relaxation volume and He-V complexes may have either positive or negative relaxation volume and increase of H/V ratio should lead to increase the relaxation volume. In the case of our experiment, after helium implantation at both temperatures the downshift may indicate dominance of defects with the positive relaxation volume: SIA and their complexes, or, following the example of tungsten [87], complexes of vacancies with helium with high He to vacancy ratio (more than 3 in the case of tungsten [87]). Therefore, it is possible to suggest that the difference in magnitude of the band shift may indicate a larger concentration of crystal defects with the positive relaxation volume (complexes of SIA) and/or higher He to vacancy ratio in bubbles. Both scenario agrees with the observed increased irradiation induced hardening of the lower temperature irradiated samples.

The increased radiation induced hardening of the lower-purity grade after exposure at 200°C may possible originate from an influence of impurities on redistribution of helium or point defects, however, creation of impurity clusters which act as obstacles for dislocations could be also considered. The chemistry effect on radiation resistance of beryllium was never systematically studied, and the available data is scattered. For example, similarly to our observation, Kupriyanov et al [55] demonstrated that after neutron irradiation in CM-3 reactor at 130-180ºC the lower purity TIP-30 and TE-30 beryllium grades experienced a higher radiation-induced increase of the yield strength than the higher purity TshG-56. However, the results of Snead [73] demonstrated lower irradiation induced hardening of the lower purity P0 grade than of the higher purity S-65C grade irradiated in the high flux beam reactor (BNL) at temperatures between 105 and 275ºC.

Currently, the high purity S-65C grade has been selected as the reference plasma-facing material in ITER on the basis of its excellent thermal fatigue and thermal shock behavior, and a good available database on its properties [7]. Our results support this choice, demonstrating that at a helium content that corresponds to the end-of-life of plasma-facing beryllium in ITER [16], the properties of this grade exhibit higher radiation stability, e.g. smaller radiation-induced hardening than the lower purity grade. However, the mechanism(s) responsible for this are not known. A detailed fine scale high resolution TEM analysis, complimented by fine scale chemical analysis, for example with Atom Probe Tomography, and preferably Positron Annihilation Spectroscopy to elucidate the helium atom distribution, would be required to understand the hardening mechanisms from individual features in the irradiated microstructure.

The results are also important for the particle accelerator community. The irradiation conditions and hardening effects used is this study represent the average operating temperatures of beryllium windows in the operating NuMI beamline (50ºC) [18] and the currently-designed LBNF (200ºC) [9,10]. So far, the high purity PF-60 grade (similar purity to S-65, but with different grain size and texture) has been successfully used as a beam window material in the NuMI beamline, accumulating during operation up to 2000 appm of helium [18]. The result of this work demonstrate that in the future LBNF, the similar pure grade exposed to comparable doses to NuMI, but at higher temperature (200ºC), should undergo smaller radiation-induced hardening and that accumulation of up to 3000 appm of helium at this temperature does not lead to creation of cavities or bubbles (including at grain boundaries) which are known be often responsible for the severe loss of ductility in beryllium.

5. Conclusion

Two industrial beryllium grades, higher-purity S-65 and lower-purity S-200-F, were investigated in the as-received state and after helium implantation at 50 and 200ºC. The main conclusions that can be drawn from this work can be summarized as:

- At both temperatures in both grades, under TEM investigation the radiation damage appears as “black dots” (<10 nm in diameter) which are likely to be small dislocation loops with the number density of ~ 10^{22} m^{-3}. No bubbles were observed inside grains and at grain boundaries.
- The lower-purity S-200-F grade has higher average hardness (3.7±0.8 GPa) than the S-65 grade (3.4±0.8 GPa) in the as-received state and remained harder after helium implantations. In both grades the implantation at 50ºC almost doubled the average hardness, and at 200ºC led to a 60% hardness increase, compared to the average hardness of the unimplanted material.
- By combining nanoindentation with EBSD it was possible to separate out the influence of crystal orientation on hardness. In the as-received materials the hardness is about 2.5 times higher when the indentation direction is close to the [0001] c-axis of beryllium, compared to indentation perpendicular to [0001]. Grades with “soft orientation” were most sensitive to radiation induced hardening, which increased almost 3 times after 50ºC implantation and 2 times after exposure at 200ºC. The higher purity grade S-65 had a 12% smaller increase of the “soft orientation” hardness at 200ºC then the less S-200-F. Hardness anisotropy significantly decreased after helium implantation as “hard orientation” hardness values were less affected by radiation .
- Near-indentation surface topography, which is not accounted for in the standard “Oliver-Phaar” analysis, can have a strong influence on the extraction of true hardness values from nanoindentation data. A combination of nanoindentation

with EBSD, to give a contact area correction, is an important procedure in such cases, for example here in the investigation of radiation damage effects in different beryllium grades.

- Topography mapping of indentation prints demonstrated that localised surface deformation around indents (pile-up and sink-in) is highly crystallographically dependent in the as-received state (sink-in behaviour dominated in hard grains close to the *c*-axis while pile-ups dominated in soft grains orthogonal to the c axis). After implantation this crystallographic dependence of topography is less prominent and either pile-ups or sink-ins may be observed. TEM and Raman microscopy indicate that whether either pile-ups or sink-ins occur in a particular specimen can be related to the detailed layered substructure of the implanted material: when the surface layer is softer (with smaller helium content) pile-ups are mainly observed, while in the opposite case (harder surface layer with higher helium content) sink-ins are dominant.
- Analysis of the possible hardening contribution demonstrated that the "back dots" at calculated number densities could be responsible for up to half of the observed hardening, while the rest should originate from helium bubbles with the size below the TEM resolution (<1…1.5 nm). It is expected that the bubbles are relatively weak obstacles with the strengthening factor $\alpha < 0.2$. Solid solution hardening by helium atoms is unlikely to significantly contribute to the observed hardness increase.

6. Acknowledgments

This work was supported by the Fermi Research Alliance, LLC under Contract No. DE-AC02-07CH11359 with the United States Department of Energy, and by the UK Science and

Technology Facilities Council. This work was also partially funded by the RCUK Energy Programme (Grant No. EP/T012250/1). The research used UKAEA's Materials Research Facility, which has been funded by and is part of the UK's National Nuclear User Facility and Henry Royce Institute for Advanced Materials.

The authors also acknowledge the support of the EPSRC Advanced Nuclear Materials Platform grant (Grant No. EP/P001645/1).

7. References

[1] D.M. Duffy, Fusion power: a challenge for materials science, Philos. Trans. R. Soc. Math. Phys. Eng. Sci. 368 (2010) 3315–3328. https://doi.org/10.1098/rsta.2010.0060.

[2] C. Thomser, V. Bailescu, S. BREZINSEK, J.W. COENEN, H. GREUNER, T. HIRAI, J. LINKE, C.P. LUNGU, H. MAIER, G. MATTHEWS, P. MERTENS, R. NEU, V. PHILIPPS, V. RICCARDO, M. RUBEL, C. RUSET, A. SCHMIDT, I. UYTDENHOUWEN, PLASMA FACING MATERIALS FOR THE JET ITER-LIKE WALL, 62 (2012) 8.

[3] E.B. Deksnis, A.T. Peacock, H. Altmann, C. Ibbot, H.D. Falter, Beryllium plasma-facing components: JET experience, Fusion Eng. Des. 37 (1997) 515–530. https://doi.org/10.1016/S0920-3796(97)00093-8.

[4] F. Elio, K. Ioki, P. Barabaschi, L. Bruno, A. Cardella, M. Hechler, T. Kodama, A. Lodato, D. Loesser, D. Lousteau, N. Miki, K. Mohri, R. Parker, R. Raffray, D. Williamson, M. Yamada, W. Daenner, R. Mattas, Y. Strebkov, H. Takatsu, Engineering design of the ITER blanket and relevant research and development results, Fusion Eng. Des. 46 (1999) 159–175. https://doi.org/10.1016/S0920-3796(99)00043-5.

[5] M. Merola, F. Escourbiac, R. Raffray, P. Chappuis, T. Hirai, A. Martin, Overview and status of ITER internal components, Fusion Eng. Des. 89 (2014) 890–895. https://doi.org/10.1016/j.fusengdes.2014.01.055.

[6] P. Vladimirov, D. Bachurin, V. Borodin, V. Chakin, M. Ganchenkova, A. Fedorov, M. Klimenkov, I. Kupriyanov, A. Moeslang, M. Nakamichi, T. Shibayama, S. Van Til, M. Zmitko, Current Status of Beryllium Materials for Fusion Blanket Applications, Fusion Sci. Technol. 66 (2014) 28–37. https://doi.org/10.13182/FST13-776.

[7] G. Federici, R. Doerner, P. Lorenzetto, V. Barabash, Beryllium as a Plasma-Facing Material for Near-Term Fusion Devices., Compr. Nucl. Mater. Vol 4 Radiat. Eff. Struct. Funct. Mater. Fission Fusion React. 2012 P 621-666 Elsevier Ref. Module Mater. Sci. Mater. Eng. 4 (2012) 621–666. https://doi.org/10.1016/B978-0-08-056033-5.00121-X.

[8] P. Hurh, K. Ammigan, B. Hartsell, R. Tschirhart, Targetry Challenges at Megawatt Proton Accelerator Facilities, THPFI083, Proceedings of the 4th International Particle Accelerator Conference, (2013).

[9] T. Davenne, O. Caretta, C. Densham, M. Fitton, P. Loveridge, P. Hurh, R. Zwaska, J. Hylen, V. Papadimitriou, Segmented beryllium target for a 2 MW super beam facility, Phys. Rev. Spec. Top. - Accel. Beams. 18 (2015) 091003. https://doi.org/10.1103/PhysRevSTAB.18.091003.

[10] J. Strait, E. McCluskey, T. Lundin, J. Willhite, T. Hamernik, V. Papadimitriou, A. Marchionni, M.J. Kim, M. Nessi, D. Montanari, A. Heavey, Long-Baseline Neutrino Facility (LBNF) and Deep Underground Neutrino Experiment (DUNE) Conceptual

Design Report Volume 3: Long-Baseline Neutrino Facility for DUNE June 24, 2015, ArXiv160105823 Hep-Ex Physicsphysics. (2016). http://arxiv.org/abs/1601.05823 (accessed December 5, 2016).
[11] M. Klimenkov, V. Chakin, A. Moeslang, R. Rolli, TEM study of beryllium pebbles after neutron irradiation up to 3000 appm helium production, J. Nucl. Mater. 443 (2013) 409–416. https://doi.org/10.1016/j.jnucmat.2013.07.050.
[12] I.B. Kupriyanov, V.A. Gorokhov, R.R. Melder, Z.E. Ostrovsky, A.A. Gervash, Investigation of ITER candidate beryllium grades irradiated at high temperature, J. Nucl. Mater. 258–263, Part 1 (1998) 808–813. https://doi.org/10.1016/S0022-3115(98)00383-3.
[13] V. Chakin, J. Reimann, A. Moeslang, R. Latypov, A. Obukhov, Thermal conductivity of highly neutron-irradiated beryllium in nuclear fusion reactors, Prog. Nucl. Energy. 57 (2012) 2–7. https://doi.org/10.1016/j.pnucene.2011.11.011.
[14] M.R. Gilbert, J.-C. Sublet, R.A. Forrest, Handbook of activation, transmutation, and radiation damage properties of the elements simulated using FISPACT-II and TENDL-2015 - Magnetic Fusion Plants, 2015.
[15] M.E. Sawan, Damage parameters of structural materials in fusion environment compared to fission reactor irradiation, Fusion Eng. Des. 87 (2012) 551–555. https://doi.org/10.1016/j.fusengdes.2012.01.022.
[16] V. Barabash, Material / plasma surface interaction issues following neutron damage, J. Nucl. Mater. 316 (2003) 42–51.
[17] E. Proust, L. Anzidei, G. Casini, M.D. Donne, L. Giancarli, S. Malang, Breeding blanket for DEMO, Fusion Eng. Des. 22 (1993) 19–33. https://doi.org/10.1016/S0920-3796(05)80005-5.
[18] V. Kuksenko, K. Ammigan, B. Hartsell, C. Densham, P. Hurh, S. Roberts, Irradiation effects in beryllium exposed to high energy protons of the NuMI neutrino source, J. Nucl. Mater. 490 (2017) 260–271. https://doi.org/10.1016/j.jnucmat.2017.04.011.
[19] D.S. Gelles, H.L. Heinisch, Neutron damage in beryllium, J. Nucl. Mater. 191–194, Part A (1992) 194–198. https://doi.org/10.1016/S0022-3115(09)80032-9.
[20] V.P. Chakin, A.O. Posevin, R.N. Latypov, Radiation damage in beryllium at 70–440°C and neutron fluence (0.3–18)·1022 cm−2 (E n > 0.1 MeV), At. Energy. 101 (2006) 743–749. https://doi.org/10.1007/s10512-006-0162-9.
[21] V.P. Chakin, A.O. Posevin, A.V. Obukhov, P.P. Silantyev, Radiation growth of beryllium, J. Nucl. Mater. 386–388 (2009) 206–209. https://doi.org/10.1016/j.jnucmat.2008.12.097.
[22] S.A. Fabritsiev, A.S. Pokrovsky, R.M. Bagautdinov, Neutron irradiation effect on the mechanical properties and structure of beryllium, ResearchGate. (1999) 1062–1076.
[23] A.S. Pokrovsky, S.A. Fabritsiev, R.M. Bagautdinov, Yu.D. Goncharenko, High-temperature beryllium embrittlement, J. Nucl. Mater. 233–237, Part 2 (1996) 841–846. https://doi.org/10.1016/S0022-3115(96)00027-X.
[24] W. Kesternich, H. Ullmaier, Mechanical properties and microstructure of helium-implanted beryllium, J. Nucl. Mater. 312 (2003) 212–223. https://doi.org/10.1016/S0022-3115(02)01637-9.
[25] Beryllium Science and Technology., Springer Verlag, 2012.
[26] C. Dorn, K. Tsuchiya, Y. Hatano, P. Chakrov, M. Kodama, H. Kawamura, Development of beryllium material for reflector lifetime expansion, in: Proc. 5th Int. Symp. Mater. Test. React. ISMTR-5, Columbia, 2012. https://jopss.jaea.go.jp/search/servlet/search?5038030&language=1 (accessed December 30, 2019).

[27] C.D. Hardie, S.G. Roberts, A.J. Bushby, Understanding the effects of ion irradiation using nanoindentation techniques, J. Nucl. Mater. 462 (2015) 391–401. https://doi.org/10.1016/j.jnucmat.2014.11.066.
[28] C. Heintze, F. Bergner, S. Akhmadaliev, E. Altstadt, Ion irradiation combined with nanoindentation as a screening test procedure for irradiation hardening, J. Nucl. Mater. 472 (2016) 196–205. https://doi.org/10.1016/j.jnucmat.2015.07.023.
[29] D.L. Krumwiede, T. Yamamoto, T.A. Saleh, S.A. Maloy, G.R. Odette, P. Hosemann, Direct comparison of nanoindentation and tensile test results on reactor-irradiated materials, J. Nucl. Mater. 504 (2018) 135–143. https://doi.org/10.1016/j.jnucmat.2018.03.021.
[30] A. Reichardt, A. Lupinacci, D. Frazer, N. Bailey, H. Vo, C. Howard, Z. Jiao, A.M. Minor, P. Chou, P. Hosemann, Nanoindentation and in situ microcompression in different dose regimes of proton beam irradiated 304 SS, J. Nucl. Mater. 486 (2017) 323–331. https://doi.org/10.1016/j.jnucmat.2017.01.036.
[31] J. Jiang, Y.C. Wu, X.B. Liu, R.S. Wang, Y. Nagai, K. Inoue, Y. Shimizu, T. Toyama, Microstructural evolution of RPV steels under proton and ion irradiation studied by positron annihilation spectroscopy, J. Nucl. Mater. 458 (2015) 326–334. https://doi.org/10.1016/j.jnucmat.2014.12.113.
[32] P. Song, D. Morrall, Z. Zhang, K. Yabuuchi, A. Kimura, Radiation response of ODS ferritic steels with different oxide particles under ion-irradiation at 550 °C, J. Nucl. Mater. 502 (2018) 76–85. https://doi.org/10.1016/j.jnucmat.2018.02.007.
[33] C.E. Beck, F. Hofmann, J.K. Eliason, Alexei.A. Maznev, K.A. Nelson, D.E.J. Armstrong, Correcting for contact area changes in nanoindentation using surface acoustic waves, Scr. Mater. 128 (2017) 83–86. https://doi.org/10.1016/j.scriptamat.2016.09.037.
[34] O. El-Atwani, J.S. Weaver, E. Esquivel, M. Efe, M.R. Chancey, Y.Q. Wang, S.A. Maloy, N. Mara, Nanohardness measurements of heavy ion irradiated coarse- and nanocrystalline-grained tungsten at room and high temperature, J. Nucl. Mater. 509 (2018) 276–284. https://doi.org/10.1016/j.jnucmat.2018.06.023.
[35] V. Kuksenko, S.G. Roberts, E. Tarleton, The hardness and modulus of polycrystalline beryllium from nano-indentation, Int. J. Plast. (2018). https://doi.org/10.1016/j.ijplas.2018.12.008.
[36] G.P. Walters, Effect of neutron irradiation on the mechanical properties of hot-pressed and extruded beryllium, J. Common Met. 11 (1966) 77–88. https://doi.org/10.1016/0022-5088(66)90072-5.
[37] K.A. Walsh, Beryllium Chemistry and Processing, ASM International, 2009.
[38] M. Knezevic, I.J. Beyerlein, D.W. Brown, T.A. Sisneros, C.N. Tomé, A polycrystal plasticity model for predicting mechanical response and texture evolution during strain-path changes: Application to beryllium, Int. J. Plast. 49 (2013) 185–198. https://doi.org/10.1016/j.ijplas.2013.03.008.
[39] N.A. Hill, J.W.S. Jones, The crystallographic dependence of low load indentation hardness in beryllium, J. Nucl. Mater. 3 (1961) 138–155. https://doi.org/10.1016/0022-3115(61)90002-2.
[40] K. Tsuya, The effect of temperature on the hardness anisotropy of beryllium single crystals, J. Nucl. Mater. 22 (1967) 148–157. https://doi.org/10.1016/0022-3115(67)90024-4.
[41] S-65 Nuclear Grade Beryllium - Materion - https://materion.com/Products/Beryllium/Beryllium-Metal/S-65.aspx, (2018). https://materion.com/Products/Beryllium/Beryllium-Metal/S-65.aspx.

[42] S-200-F Vacuum Hot Pressed Beryllium - Materion - https://materion.com/Products/Beryllium/Beryllium-Metal/S-200F.aspx, (2018). https://materion.com/Products/Beryllium/Beryllium-Metal/S-200F.aspx.
[43] J.F. (James F.) Ziegler, U. Littmark, J.P. Biersack, The stopping and range of ions in solids / J.F. Ziegler, J.P. Biersack, U. Littmark, Pergamon, New York, 1985.
[44] J.F. Ziegler, M.D. Ziegler, J.P. Biersack, SRIM – The stopping and range of ions in matter (2010), Nucl. Instrum. Methods Phys. Res. Sect. B Beam Interact. Mater. At. 268 (2010) 1818–1823. https://doi.org/10.1016/j.nimb.2010.02.091.
[45] L.R. Greenwood, R.K. Smither, SPECTER: neutron damage calculations for materials irradiations, Argonne National Lab., IL (USA), 1985. http://inis.iaea.org/Search/search.aspx?orig_q=RN:16073192 (accessed July 8, 2014).
[46] W.C. Oliver, G.M. Pharr, An improved technique for determining hardness and elastic modulus using load and displacement sensing indentation experiments, J. Mater. Res. 7 (1992) 1564–1583. https://doi.org/10.1557/JMR.1992.1564.
[47] Gwyddion – Applications - http://gwyddion.net/, (2018). http://gwyddion.net/ (accessed October 23, 2017).
[48] ISO 14577-1:2015. Metallic materials -- Instrumented indentation test for hardness and materials parameters -- Part 1: Test method, 2nd ed., ISO Central Secretariat, Geneva, Switzerland, 2015.
[49] K.O. Kese, Z.C. Li, B. Bergman, Method to account for true contact area in soda-lime glass during nanoindentation with the Berkovich tip, Mater. Sci. Eng. A. 404 (2005) 1–8. https://doi.org/10.1016/j.msea.2005.06.006.
[50] A.C. Fischer-Cripps, Nanoindentation, Springer New York, New York, NY, 2004. https://doi.org/10.1007/978-1-4757-5943-3.
[51] OIM Analysis™/ EDAX, (2018). https://www.edax.com/products/ebsd/oim-analysis (accessed April 9, 2018).
[52] M.I. Rusu, C. Pardanaud, Y. Ferro, G. Giacometti, C. Martin, Y. Addab, P. Roubin, M. Minissale, L. Ferri, F. Virot, M. Barrachin, C.P. Lungu, C. Porosnicu, P. Dinca, M. Lungu, M. Köppen, P. Hansen, C. Linsmeier, Preparing the future post-mortem analysis of beryllium-based JET and ITER samples by multi-wavelengths Raman spectroscopy on implanted Be, and co-deposited Be, Nucl. Fusion. 57 (2017) 076035. https://doi.org/10.1088/1741-4326/aa70bb.
[53] M.L. Jenkins, M.A. Kirk, Characterisation of Radiation Damage by Transmission Electron Microscopy, 1st ed., Taylor & Francis, 2000.
[54] M. Klimenkov, P. Vladimirov, J. Hoffmann, N. Zimber, A. Möslang, V. Kuksenko, First simultaneous detection of helium and tritium inside bubbles in beryllium, Micron. (2019) 102754. https://doi.org/10.1016/j.micron.2019.102754.
[55] I.B. Kupriyanov, R.R. Melder, V.A. Gorokhov, The effect of neutron irradiation on beryllium performance, Fusion Eng. Des. 51–52 (2000) 135–143. https://doi.org/10.1016/S0920-3796(00)00306-9.
[56] L. Coheur, Cayphas, J.-M., Delavignette, P, Hou, M., Microstructural effects of neutron irradiation in beryllium, (1999).
[57] V.P. Chakin, A.O. Posevin, I.B. Kupriyanov, Swelling, mechanical properties and microstructure of beryllium irradiated at 200°C up to extremely high neutron doses, J. Nucl. Mater. 367–370 (2007) 1377–1381. https://doi.org/10.1016/j.jnucmat.2007.03.253.
[58] K. Morishita, T. Inoue, N. Yoshida, Microstructural evolution in beryllium by fusion-relevant low energy helium ion irradiation, J. Nucl. Mater. 266–269 (1999) 997–1002. https://doi.org/10.1016/S0022-3115(98)00879-4.

[59] A. Bolshakov, G.M. Pharr, Influences of pileup on the measurement of mechanical properties by load and depth sensing indentation techniques, J. Mater. Res. 13 (1998) 1049–1058. https://doi.org/10.1557/JMR.1998.0146.
[60] K.W. McElhaney, J.J. Vlassak, W.D. Nix, Determination of indenter tip geometry and indentation contact area for depth-sensing indentation experiments, J. Mater. Res. 13 (1998) 1300–1306. https://doi.org/10.1557/JMR.1998.0185.
[61] D. Lorenz, A. Zeckzer, U. Hilpert, P. Grau, H. Johansen, H.S. Leipner, Pop-in effect as homogeneous nucleation of dislocations during nanoindentation, in: 2003. https://doi.org/10.1103/PhysRevB.67.172101.
[62] E.T. Lilleodden, W.D. Nix, Microstructural length-scale effects in the nanoindentation behavior of thin gold films, Acta Mater. 54 (2006) 1583–1593. https://doi.org/10.1016/j.actamat.2005.11.025.
[63] F. Pöhl, Pop-in behavior and elastic-to-plastic transition of polycrystalline pure iron during sharp nanoindentation, Sci. Rep. 9 (2019) 1–12. https://doi.org/10.1038/s41598-019-51644-5.
[64] J.S. Weaver, C. Sun, Y. Wang, S.R. Kalidindi, R.P. Doerner, N.A. Mara, S. Pathak, Quantifying the mechanical effects of He, W and He + W ion irradiation on tungsten with spherical nanoindentation, J. Mater. Sci. 53 (2018) 5296–5316. https://doi.org/10.1007/s10853-017-1833-8.
[65] T.B. Britton, D. Randman, A.J. Wilkinson, Nanoindentation study of slip transfer phenomenon at grain boundaries, J. Mater. Res. 24 (2009) 607–615. https://doi.org/10.1557/jmr.2009.0088.
[66] N. Tayebi, A.A. Polycarpou, T.F. Conry, Effects of substrate on determination of hardness of thin films by nanoscratch and nanoindentation techniques, J. Mater. Res. 19 (2004) 1791–1802. https://doi.org/10.1557/JMR.2004.0233.
[67] T.Y. Tsui, G.M. Pharr, Substrate effects on nanoindentation mechanical property measurement of soft films on hard substrates, J. Mater. Res. 14 (1999) 292–301. https://doi.org/10.1557/JMR.1999.0042.
[68] W.J. Evans, M.J. Lipp, H. Cynn, C.S. Yoo, M. Somayazulu, D. Häusermann, G. Shen, V. Prakapenka, X-ray diffraction and Raman studies of beryllium: Static and elastic properties at high pressures, Phys. Rev. B. 72 (2005) 094113. https://doi.org/10.1103/PhysRevB.72.094113.
[69] G. Gouadec, P. Colomban, Raman Spectroscopy of nanomaterials: How spectra relate to disorder, particle size and mechanical properties, Prog. Cryst. Growth Charact. Mater. 53 (2007) 1–56. https://doi.org/10.1016/j.pcrysgrow.2007.01.001.
[70] C. Zambaldi, Y. Yang, T.R. Bieler, D. Raabe, Orientation informed nanoindentation of α-titanium: Indentation pileup in hexagonal metals deforming by prismatic slip, J. Mater. Res. 27 (2012) 356–367. https://doi.org/10.1557/jmr.2011.334.
[71] S. Das, D.E.J. Armstrong, Y. Zayachuk, W. Liu, R. Xu, F. Hofmann, The effect of helium implantation on the deformation behaviour of tungsten: X-ray micro-diffraction and nanoindentation, Scr. Mater. 146 (2018) 335–339. https://doi.org/10.1016/j.scriptamat.2017.12.014.
[72] D.E.J. Armstrong, A.J. Wilkinson, S.G. Roberts, Mechanical properties of ion-implanted tungsten–5\hspace0.167emwt% tantalum, Phys. Scr. T145 (2011) 014076. https://doi.org/10.1088/0031-8949/2011/T145/014076.
[73] L.L. Snead, Low-temperature low-dose neutron irradiation effects on beryllium, J. Nucl. Mater. 326 (2004) 114–124. https://doi.org/10.1016/j.jnucmat.2003.12.016.
[74] D.S. Gelles, G.A. Sernyaev, M.D. Donne, H. Kawamura, Radiation effects in beryllium used for plasma protection, J. Nucl. Mater. 212–215, Part 1 (1994) 29–38. https://doi.org/10.1016/0022-3115(94)90030-2.

[75] R. Lässer, Tritium and Helium-3 in Metals, Springer-Verlag, Berlin Heidelberg, 1989. https://doi.org/10.1007/978-3-642-73510-3.
[76] N.J. Petch, E. Wright, The Plasticity and Cleavage of Polycrystalline Beryllium. I. Yield and Flow Stresses, Proc. R. Soc. Math. Phys. Eng. Sci. 370 (1980) 17–27. https://doi.org/10.1098/rspa.1980.0019.
[77] G.E. Lucas, The evolution of mechanical property change in irradiated austenitic stainless steels, J. Nucl. Mater. 206 (1993) 287–305. https://doi.org/10.1016/0022-3115(93)90129-M.
[78] L. Tan, J.T. Busby, Formulating the strength factor alpha for improved predictability of radiation hardening, J. Nucl. Mater. 465 (2015). https://doi.org/10.1016/j.jnucmat.2015.07.009.
[79] R.L. Fleischer, Substitutional solution hardening, Acta Metall. 11 (1963) 203–209. https://doi.org/10.1016/0001-6160(63)90213-X.
[80] V. Kuksenko, Experimental investigation of radiation damage effects in beryllium: updates on recent results obtained on proton, neutron and He-ions irradiated samples, (2019).
[81] K.D. Hammond, D. Maroudas, B.D. Wirth, Theoretical Model of Helium Bubble Growth and Density in Plasma-Facing Metals, Sci. Rep. 10 (2020) 2192. https://doi.org/10.1038/s41598-020-58581-8.
[82] H.M. Lu, Q. Jiang, Size-Dependent Surface Energies of Nanocrystals, (2004). https://doi.org/10.1021/jp0366264.
[83] M. Benedict, Pressure, Volume, Temperature Properties of Nitrogen at High Density. II. Results Obtained by a Piston Displacement Method, J. Am. Chem. Soc. 59 (1937) 2233–2242. https://doi.org/10.1021/ja01290a038.
[84] R.L. Mills, D.H. Liebenberg, J.C. Bronson, Equation of state and melting properties of $^{4}\mathrm{He}$ from measurements to 20 kbar, Phys. Rev. B. 21 (1980) 5137–5148. https://doi.org/10.1103/PhysRevB.21.5137.
[85] L. Peng, Y. Dai, Helium-induced hardening effect in ferritic/martensitic steels F82H and Optimax-A irradiated in a mixed spectrum of high energy protons and spallation neutrons, J. Nucl. Mater. 417 (2011) 996–1000. https://doi.org/10.1016/j.jnucmat.2010.12.208.
[86] R. Schäublin, Y.L. Chiu, Effect of helium on irradiation-induced hardening of iron: A simulation point of view, J. Nucl. Mater. 362 (2007) 152–160. https://doi.org/10.1016/j.jnucmat.2007.01.187.
[87] F. Hofmann, D. Nguyen-Manh, M.R. Gilbert, C.E. Beck, J.K. Eliason, A.A. Maznev, W. Liu, D.E.J. Armstrong, K.A. Nelson, S.L. Dudarev, Lattice swelling and modulus change in a helium-implanted tungsten alloy: X-ray micro-diffraction, surface acoustic wave measurements, and multiscale modelling, Acta Mater. 89 (2015) 352–363. https://doi.org/10.1016/j.actamat.2015.01.055.